Engineering xxx (xxxx) xxx

Contents lists available at ScienceDirect

Engineering

journal homepage: www.elsevier.com/locate/eng

Research
Sustainable and High-Performance Structural Materials—Article

A Generic Damage-Plasticity Model for Confined Concrete in Various Stress States

Yichen Lu, Guangming Chen *

State Key Laboratory of Subtropical Building and Urban Science, South China University of Technology, Guangzhou 510641, China

ARTICLE INFO

Article history:
Received 31 January 2025
Revised 8 March 2026
Accepted 8 April 2026
Available online xxxx

Keywords:
FRP
FRP-confined concrete
Active confinement
Passive confinement
Constitutive model
Non-uniform confinement
Eccentric compression
Cracking

ABSTRACT

Confined concrete has garnered significant attention owing to its advantages, such as enhanced strength, improved deformation capacity, and associated benefits when used in engineering structures. Although existing constitutive models reasonably predict the behavior of actively and passively confined concrete columns under axial compression, they are not designed to model concrete behavior in various stress states encountered in practice, including eccentrically compressed concrete columns passively confined by fiber-reinforced polymer (FRP) sheets. Accordingly, this study presents a new three-dimensional damaged-plasticity model for confined concrete under various stress states, based on the well-known Lubliner–Lee damaged-plasticity model. A key advancement involves a capped potential surface with a bulged triangular deviatoric trace under compression-dominated stress states and a Drucker–Prager potential surface under tension-dominated stress states, connected by a smooth transition. The potential surface, along with a properly designed yield surface, hardening rule, and evolution law for internal variables, makes the proposed model well suited to capturing concrete behavior under various stress states, including triaxial compression, tension–compression, and loading–unloading. The constitutive model is first validated against monotonic and cyclic axial-compression data for actively and passively confined concrete and then verified using eccentric-compression results for FRP-confined concrete. The validation confirms the capability and accuracy of the proposed model to capture concrete behavior under various stress states.

1. Introduction

Research has established that concrete exhibits enhanced strength and deformation capacity under triaxial compression. This property is utilized in confined concrete members, where concrete is encased in a confining unit. Such members are suitable as compression-dominant elements in structural systems such as main columns of wind turbine towers (Fig. 1(a)), bridge piers (Fig. 1(b)), and arch ribs of arch bridges (Fig. 1(c)). Over the past few decades, steel tubes have been widely used to confine concrete and form concrete-filled steel tube (CFST, Fig. 1(d)) members [1]. Fiber-reinforced polymers (FRPs) have been used owing to their high strength-to-weight ratio and corrosion resistance, producing FRP-confined concrete (FCC, Fig. 1(e)) members [2,3] and concrete-filled FRP tube (CFFT, Fig. 1(f)) members [4]. In these members, the lateral dilation of concrete under axial compression stretches the confining unit in the hoop direction, generating uniform confining pressure on the concrete core (Fig. 1(g)). Confining stress varies mainly with sectional geometry (circular vs noncircular) and loading conditions (axial vs eccentric). The material properties of confining components also play an important role. For example, in CFST members, confinement approaches constant pressure after full yielding of the steel tube, whereas FRP provides increasing passive confinement [5] because confining stress depends on the lateral dilation of concrete until FRP ruptures. To describe the mechanical behavior of confined concrete, one-dimensional axial stress–strain models have been developed for both actively [6] and passively [5] confined concrete, implicitly incorporating effects of lateral confinement. Compared with design-oriented models [5], analysis-oriented models [7] explicitly account for interactions between concrete dilation and axial contraction. However, because analysis-oriented models are derived from concentric compression (Fig. 1(g)), they cannot capture the effects of non-uniform confinement under eccentric loading

* Corresponding author.
E-mail address: guangmingchen@scut.edu.cn (G. Chen).

https://doi.org/10.1016/j.eng.2026.04.003

Please cite this article as: Y. Lu and G. Chen, A Generic Damage-Plasticity Model for Confined Concrete in Various Stress States, Engineering, https://doi.org/10.1016/j.eng.2026.04.003

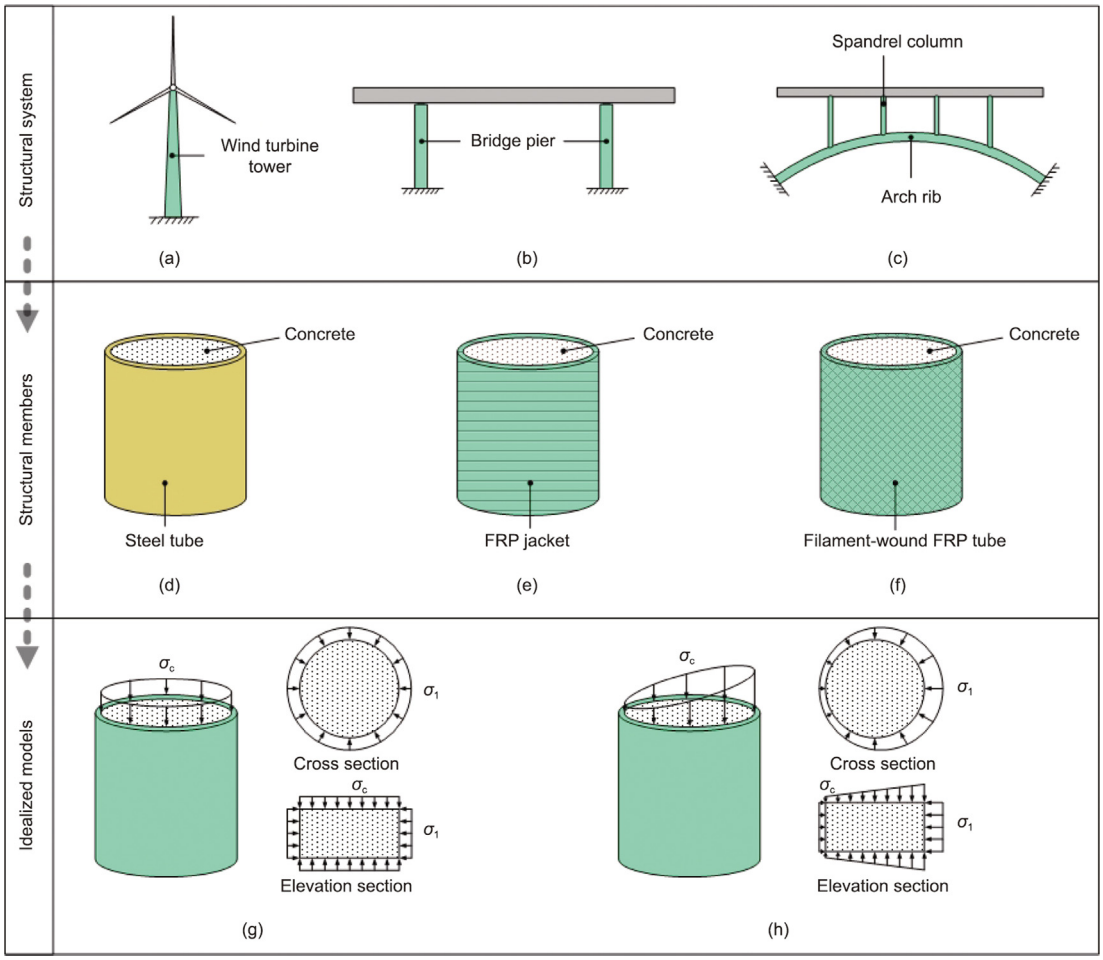

Fig. 1. Schematic of confined concrete in structural applications and under different loading conditions. (a) Wind turbine tower; (b) bridge pier; (c) arch bridge; (d) CFST members; (e) FCC members; (f) CFFT members; (g) uniform confinement under concentric compression; (h) non-uniform confinement under eccentric compression. σ_c represents axial stress, and σ_l represents lateral confining stress.

(Fig. 1(h)). Therefore, a three-dimensional constitutive model is necessary to accurately capture confined concrete behavior under complex stress states encountered in real structures (Figs. 1(a)–(c)).

The literature review in Section 2 shows that several existing models, such as those proposed by Yu et al. [8,9] and Zheng and Teng [10], partially capture confined concrete behavior under various loading conditions. However, none of these models comprehensively address the following critical issues: ① predicting plastic volumetric compaction under high confining pressure; ② capturing non-uniform concrete dilation due to non-uniform confinement; ③ modeling tensile damage behavior (including concrete cracking) under tension-dominated stress states; and ④ reflecting stiffness degradation under loading–unloading conditions. To address the limitations of existing models, this study proposes a generic damaged-plasticity constitutive model for confined concrete that simultaneously resolves the aforementioned critical issues. Therefore, the model is suitable for analyzing hybrid structures that incorporate confined concrete under complex loading conditions. The proposed model advances the work of Zheng and Teng [10] by predicting concrete cracking in tension-dominated stress states and modeling stiffness degradation through damage initiation and evolution. Furthermore, the new model is formulated with variables that can be calibrated using parameters with clear physical meanings (such as parameters determined from material or specimen test data).

Throughout this study, compressive stresses and strains are treated as negative quantities, whereas tensile stresses are regarded as positive unless otherwise specified. However, material strengths are given as absolute values in accordance with common conventions. Tensor and vector symbols are written in boldface, whereas scalar symbols are written in plain font.

2. Literature review and research significance

Active and passively confined concrete have been experimentally investigated by numerous researchers [3,7,11–13], leading to a comprehensive understanding of confined concrete mechanical behavior. As confined concrete behavior forms the basis of constitutive modeling, Section S1 in Appendix A provides a brief description of this behavior for reference.

Regarding constitutive models for confined concrete, researchers worldwide have made numerous efforts; however, most models, including those proposed by Lee and Fenves [14], Papanikolaou and Kappos [15], and Grassl et al. [16], have been developed for actively confined concrete. Early constitutive models for passively confined concrete have been designed within the framework of classical plasticity theory, incorporating key components such as yield function, hardening rule, and flow rule [17]. However, these models [18–23] offer reasonably accurate predictions only under certain conditions. To overcome existing limitations, Yu et al. [8,9] modified the concrete damaged-plasticity model (hereafter

referred to as the CDP model) available in ABAQUS (Dassault Systèmes, France) [24] to capture the behavior of uniformly confined concrete, concrete in rectangular FCC or CFFT columns, and FRP-concrete-steel double-skin tubular columns (DSTC) [7]. These modifications were implemented through user-defined field subroutines, which allowed the hardening and damage evolution laws, along with the dilation angle, to depend on confinement stiffness and confining pressure, without altering the core governing equations of the original CDP model. Consequently, certain limitations of the original CDP model [24] persist in their modified model. First, the modified CDP model cannot simulate plastic volumetric compaction under high confining pressure because its Drucker–Prager (D–P) type potential surface predicts an almost constant dilation angle. Second, the model underestimates the difference between the two principal lateral strains under strongly non-uniform confinement [25], mainly due to the circular deviatoric trace of the D–P type potential surface [10]. Third, the model deals only with monotonic loading because cyclic behavior is not accurately represented. Despite subsequent improvements by other researchers [26,27], the modified CDP model [9] still suffers from these intrinsic limitations.

The preceding discussion highlights that a potential surface with a simple linear form, such as the D–P type, is insufficient to capture full-range deformation properties of confined concrete under different stress states. Zheng and Teng [10] addressed this problem by proposing a potential surface with a capped meridian and a bulged triangular deviatoric trace. This formulation enables the plasticity model to accurately predict the behavior of both actively and passively confined concrete under uniform or non-uniform confinement. Unlike the approach adopted by Yu et al. [9], Zheng and Teng [10] incorporated confinement effects more rationally by embedding them directly into the hardening rules and potential functions. However, although the model performs well under multiaxial compression, it encounters difficulties under tension-dominated stress conditions. The logarithmic form of the potential function (Section 3.2) can lead to a numerical singularity in the tension-dominated region, necessitating an additional cutoff plane. Moreover, because the model is based solely on plasticity theory, it cannot account for the stiffness degradation that occurs during loading–unloading, which is a typical phenomenon in confined concrete under eccentric compression loading [4].

As indicated in Table 1 [9,10,26–28], each representative existing constitutive model exhibits certain capacity limitations under specific conditions owing to at least one critical issue outlined earlier. For example, in an FCC column under eccentric compression, all four issues can arise simultaneously or sequentially across different regions of a single specimen. Strong confinement can induce plastic volumetric compaction, whereas non-uniform confinement occurs in the compression zone under eccentric compression. Tension-dominant stress states can develop in the tension zone under large load eccentricity, and during loading, concrete near the neutral axis can undergo compressive unloading and tensile reloading. The model proposed in this study, with the essential aspects explained in Section 3, resolves the aforementioned critical issues simultaneously and accurately simulates confined concrete under various stress states in real structural applications (Fig. 1).

3. Proposed constitutive model

The proposed constitutive model is built on the CDP model framework in ABAQUS [29] based on plasticity and damage theories. Following plasticity theory, the total strain $\boldsymbol{\varepsilon}$ is decomposed into an elastic component $\boldsymbol{\varepsilon}^{\mathrm{e}}$ and a plastic component $\boldsymbol{\varepsilon}^{\mathrm{p}}$. Under the isotropic damage assumption [29], the stress–strain model of concrete can be expressed as:

$$\boldsymbol{\sigma} = (1-d)\boldsymbol{D}_0 : \boldsymbol{\varepsilon}^{\mathrm{e}} = (1-d)\boldsymbol{D}_0 : (\boldsymbol{\varepsilon} - \boldsymbol{\varepsilon}^{\mathrm{p}}) = \boldsymbol{D} : (\boldsymbol{\varepsilon} - \boldsymbol{\varepsilon}^{\mathrm{p}}) \tag{1}$$

$$\bar{\boldsymbol{\sigma}} = \boldsymbol{D}_0 : (\boldsymbol{\varepsilon} - \boldsymbol{\varepsilon}^{\mathrm{p}}) \tag{2}$$

$$\boldsymbol{\sigma} = (1-d)\bar{\boldsymbol{\sigma}} \tag{3}$$

where $\boldsymbol{D}_0$ is the initial (undamaged) elastic stiffness tensor; $\boldsymbol{D} = (1-d)\boldsymbol{D}_0$ is the damaged elastic stiffness; d is a scalar damage variable governing the degradation of elastic stiffness; $\bar{\boldsymbol{\sigma}}$ is the effective stress; and $\boldsymbol{\sigma}$ is the nominal stress. The definition of effective stress enables the decoupling of elastic–plastic response from the elastic damage response.

The constitutive equations described in subsequent sections are based on three fundamental effective stress invariants, including the effective hydrostatic pressure $\bar{p}$, the effective von Mises equivalent stress $\bar{q}$, and the Lode angle θ, which collectively form a $\bar{p}$–$\bar{q}$–θ coordinate system coaxial with the well-known Haigh–Westergaard coordinate system [30]. Definitions of these stress invariants and an illustration of the Haigh–Westergaard system are provided in Section S2 in Appendix A.

3.1. Yield function

In the original CDP model, the yield surface proposed by Lubliner et al. [31] and modified by Lee and Fenves [14] has been adopted as:

$$F = \frac{1}{1-\alpha}\left[\bar{q} - 3\alpha\bar{p} + \beta\left\langle\hat{\bar{\sigma}}_{\max}\right\rangle - \gamma\left\langle-\hat{\bar{\sigma}}_{\max}\right\rangle\right] - \bar{c}_{\mathrm{c}}(\kappa_{\mathrm{c}}) \tag{4}$$

where F denotes the yield function; α and γ are dimensionless constants; β is a dimensionless variable; $\hat{\bar{\sigma}}_{\max}$ is the algebraically maximum principal effective stress; and $\bar{c}_{\mathrm{c}}$ is the effective compressive hardening variable that evolves with the compressive internal variable κ_{c}. The yield function exhibits a bi-linear meridian trace and a bulged triangular deviatoric trace (Fig. 2), governed by parameters α, β, and γ. The coefficient α and β are defined as:

$$\alpha = \frac{k_{\mathrm{b}}-1}{2k_{\mathrm{b}}-1} \tag{5}$$

$$\beta = (1-\alpha)\frac{\bar{c}_{\mathrm{c}}(\kappa_{\mathrm{c}})}{\bar{c}_{\mathrm{t}}(\kappa_{\mathrm{t}})} - (1+\alpha) \tag{6}$$

where $k_{\mathrm{b}} = f_{\mathrm{bo}}/f_{\mathrm{co}}$ represents the ratio of the equal-biaxial compressive strength (f_{bo}) to the uniaxial compressive strength (f_{co}), and $\bar{c}_{\mathrm{t}}$ is the effective tensile hardening variable that evolves with the tensile internal variable κ_{t}.

Table 1
Main features/capacities of representative constitutive models.

Reference	Model type	Volumetric compaction	Non-uniform confinement	Tension-dominant stress states	Stiffness degradation
Zheng and Teng [10]	Plasticity	Yes	Yes	No	No
Yu et al. [9]	Damaged plasticity	No	Yes	Yes	Yes
Hany et al. [26]	Damaged plasticity	No	Yes	Yes	Yes
Mohammadi and Wu [27]	Damaged plasticity	No	Yes	Yes	Yes
Farahmandpour et al. [28]	Damaged plasticity	Yes	No	No	Yes
Proposed model	Damaged plasticity	Yes	Yes	Yes	Yes

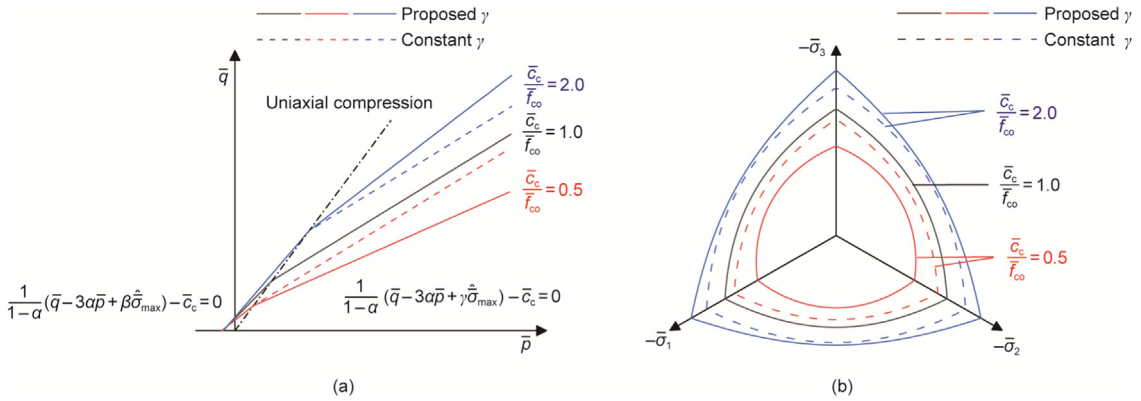

Fig. 2. Evolution of the proposed yield surface versus the Lubliner–Lee yield surface in (a) compressive meridian plane and (b) deviatoric plane at $\bar{p}=2\bar{c}_c.\bar{f}_{co}$ represents the effective compressive cylinder strength of unconfined concrete; $\bar{\sigma}_1$, $\bar{\sigma}_2$, and $\bar{\sigma}_3$ represent the principal effective stresses.

At a given effective hydrostatic pressure $\bar{p}$, let $K^F=\bar{q}^F_{TM}/\bar{q}^F_{CM}$ denote the ratio of the von Mises equivalent effective stress along the tensile meridian ($\bar{q}^F_{TM}$) to that along the compressive meridian ($\bar{q}^F_{CM}$). Since both quantities are constrained by the yield function, K^F can be defined in terms of γ as

$$K^F=\frac{\gamma+3}{2\gamma+3} \tag{7}$$

The coefficient γ enters the yield function only when $\hat{\sigma}_{max}<0$ (under triaxial compression) and influences the deviatoric trace of the yield surface. When γ is held constant, K^F remains unchanged during yield surface evolution, implying an invariant deviatoric trace.

Yu et al. [9] calibrated γ using the stress state at peak axial stress (transition state) under active confinement (Section S3 in Appendix A), yielding

$$\gamma=(1-\alpha)k_s-(1+2\alpha) \tag{8}$$

where k_s denotes the confinement effectiveness coefficient. Although this formulation captures the transition state well, it tends to overestimate the initial yield stress under high confining pressures. In this study, the proposed model preserves the original equation of the Lubliner–Lee yield function (Eq. (4)) but modifies γ to vary with κ_c.

$$\gamma=(1-\alpha)k_s\sqrt{\frac{\bar{c}_c(\kappa_c)}{\bar{f}_{co}}}-(1+2\alpha) \tag{9}$$

where $\bar{f}_{co}$ denotes the effective compressive cylinder strength of unconfined concrete (Section 4.1.4). With this modification, γ increases during loading. The parameter reduces to Eq. (8) in the transition state, while taking a lower value at the initial yield to avoid overestimation under strong confinement. As illustrated in Fig. 2(a), the original Lubliner–Lee yield surface with constant γ exhibits a steeper meridian trace, overestimating yield strength in the pre-transition region. The proposed formulation results in a lower slope and an increasingly steeper trace, similar to the evolution of the William–Warnke yield surface [32]. Correspondingly, the deviatoric trace evolves from a circular shape to a triangular one (Fig. 2(b)), consistent with the William–Warnke surface [32]. Herein, Eq. (7) implies that $\gamma<0$ corresponds to $K^F>1$, which is physically unreasonable because it implies a higher shear strength along the tensile meridian than along the compressive meridian, a condition impossible for concrete. Therefore, $\gamma\geq 0$ must hold, leading to an inequality derived from Eq. (9) as:

$$\bar{c}_{c0}\geq\left(\frac{1+2\alpha}{1-\alpha}\right)^2\cdot\frac{\bar{f}_{co}}{k_s^2} \tag{10}$$

where $\bar{c}_{c0}$ is the compressive hardening variable at initial yielding, which is equal to the initial uniaxial compressive yield stress σ_{c0} in magnitude.

In summary, when γ is dependent on κ_c, the modified yield surface evolves similarly to the William–Warnke yield surface and improves strength prediction. Lei et al. [33] proposed a different modification of the Lubliner–Lee yield function, deriving a hydrostatic pressure-dependent K^F from the William–Warnke function. However, their formulation is considerably more complex and overestimates the initial yield stress under a high active confining stress. Conversely, Eq. (9) proposed herein is much simpler and performs well under strong active confinement, as demonstrated in Section 6.1.

3.2. Potential function

In the original CDP model [29], the plastic strain rate $\dot{\boldsymbol{\varepsilon}}^p$ is determined by a non-associated flow rule with the potential function taking a simple D–P form as:

$$\dot{\boldsymbol{\varepsilon}}^p=\dot{\lambda}\frac{\partial G}{\partial\bar{\boldsymbol{\sigma}}} \tag{11}$$

$$G=\bar{q}-\bar{p}\tan\phi_c \tag{12}$$

where G is the potential function; $\dot{\lambda}$ is the plastic multiplier; and ϕ_c is a constant dilation angle. However, this form cannot capture the evolving dilation behavior of concrete under strong or non-uniform confinement, as discussed in Section 2. In this study, G is enhanced for the proposed model to better represent concrete dilation behavior. The improvements are categorized for volumetric (meridian) and deviatoric components.

3.2.1. Volumetric components

To accurately predict plastic volumetric compaction under strong confinement, the proposed model adopts a capped potential surface following the form used by Zheng and Teng [10], originally proposed by Pietruszczak et al. [34] and applied by Farahmandpour et al. [28]. However, because their formulation was based on nominal stress and a single internal state variable within a plasticity framework, modifications are required to ensure compatibility with the present damaged-plasticity model. The modified potential function in the compression-dominated region (Fig. 3(a)) can be expressed as:

$$G=\bar{q}+A\left[B\bar{f}_{co}+\bar{p}\right]\ln\frac{B\bar{f}_{co}+\bar{p}}{I_0} \tag{13}$$

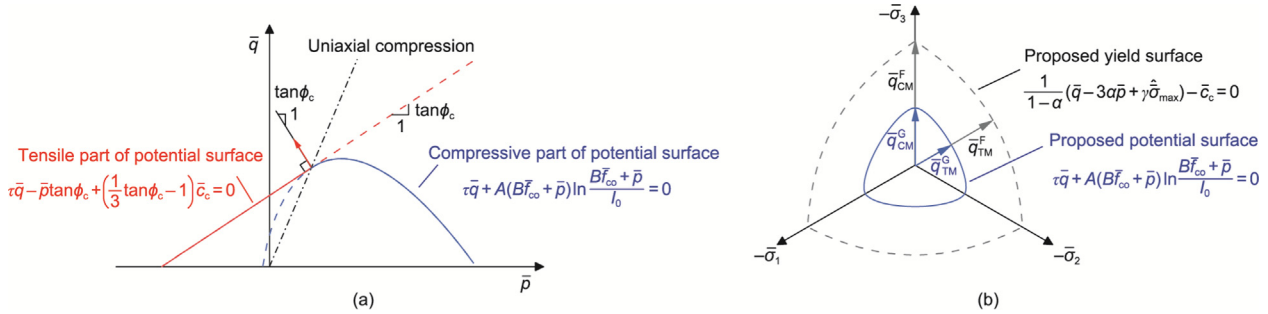

Fig. 3. Proposed potential surface in the (a) compressive meridian plane and (b) deviatoric plane. τ is a deviatoric shape function; $\bar{q}^{G}_{TM}$ and $\bar{q}^{G}_{CM}$ represent the polar lengths along the tensile and compressive meridians, respectively.

where A and B represent the shape-controlling parameters of the potential surface, and I_0 denotes the parameter that ensures stress state on the potential surface ($G = 0$).

Zheng and Teng [10] controlled dilation angle evolution during loading using parameters A and B. Their approach defined the evolution functions for A and B and calibrated them with test data, an indirect process that typically requires trial and error. In this study, the meridian shape of the potential surface is linked to a dilation angle parameter ϕ_c that evolves with κ_c, representing the varying dilation angle of unconfined concrete under uniaxial compression. According to the definition in Section S4 in Appendix A, the dilation angle (ϕ) at a given stress state can be expressed as:

$$\tan\phi = -A + \frac{\bar{q}}{B\bar{f}_{co}+\bar{p}} \tag{14}$$

To derive the expression for parameter A, the special case of unconfined concrete under uniaxial compression is considered, with principal effective stresses defined as $\bar{\sigma}_1 = \bar{\sigma}_2 = 0$ and $\bar{\sigma}_3 = -\bar{c}_c$. Under uniaxial compression, the effective axial stress equals $\bar{c}_c$ in magnitude according to the yield function. Thus, the stress invariants are defined as $\bar{q} = \bar{c}_c$ and $\bar{p} = \bar{c}_c/3$. Substituting these invariants and ϕ_c into Eq. (14) yields

$$A = \frac{\bar{c}_c(\kappa_c)}{B\bar{f}_{co}+\bar{c}_c(\kappa_c)/3} - \tan\phi_c(\kappa_c) \tag{15}$$

The evolution of ϕ_c can be calibrated using the lateral–axial strain curve derived from the uniaxial compression test (or model prediction). Parameter B, which controls the decrease in dilation angle with increasing hydrostatic pressure, is defined in this study as:

$$B = \frac{k_b}{k_b+1}\cdot\frac{\bar{c}_t(\kappa_t)}{\bar{f}_{co}} \tag{16}$$

However, the logarithmic functions in Eq. (13) are undefined for $\bar{p} \le -B\bar{f}_{co}$, a condition inevitably encountered under tension-dominated stress states. To resolve this issue, a D–P type potential surface of the form given in Eq. (12) is adopted in the tension-dominated region. Combining Eq. (12) with Eq. (13) yields the potential function proposed in this study as:

$$G = \begin{cases} \bar{q} - \bar{p}\tan\phi_c(\kappa_c) + \left[\frac{1}{3}\tan\phi_c(\kappa_c) - 1\right]\cdot\bar{c}_c(\kappa_c), & L \ge 0 \\ \bar{q} + A\left[B\bar{f}_{co} + \bar{p}\right]\cdot\ln\frac{B\bar{f}_{co}+\bar{p}}{I_0}, & L < 0 \end{cases} \tag{17}$$

where L defines a condition ensuring a continuous and smooth transition between the two potential surfaces at $\phi = \phi_c$. Substituting $\phi = \phi_c$ into Eq. (14), and rearranging the terms yields the transition criterion expressed as:

$$L = \bar{q} - \left[A + \tan\phi_c(\kappa_c)\right]\cdot\left[B\bar{f}_{co} + \bar{p}\right] = 0 \tag{18}$$

In the compressive meridian plane (Fig. 3(a)), Eq. (18) describes a straight line coinciding with the stress path of the uniaxial compression. Consequently, the shapes of both tensile ($L \ge 0$) and compressive ($L < 0$) components of the potential surface are governed by $\phi_c(\kappa_c)$.

In summary, introducing the stress-state transition function L enables the newly developed potential surface to handle both tension and compression-dominated stress states, thereby extending the range of applicable stress conditions. This represents a key advancement over the model proposed by Zheng and Teng [10]. Furthermore, the proposed expressions for A and B allow potential surface evolution to be calibrated directly using the dilation angle of unconfined concrete under uniaxial compression, making the surface more flexible and easier to calibrate.

3.2.2. Deviatoric components

The θ-independent D–P type potential surface adopted in the original CDP model [29] tends to underestimate the non-uniformity of concrete dilation under non-uniform confinement, as demonstrated by Mohammadi and Wu [25]. To address this issue, Zheng and Teng [10] proposed a potential surface with a bulged triangular deviatoric trace. This shape captures concrete dilation under non-uniform confinement more accurately and maintains a convex deviatoric trace, thereby avoiding the numerical issues associated with concave shapes. By introducing a deviatoric shape function τ as proposed by Zheng and Teng [10], the potential function in Eq. (17) can be further modified as:

$$G = \begin{cases} \tau\bar{q} - \bar{p}\tan\phi_c(\kappa_c) + \left[\frac{1}{3}\tan\phi_c(\kappa_c) - 1\right]\cdot\bar{c}_c(\kappa_c), & L \ge 0 \\ \tau\bar{q} + A\left[B\bar{f}_{co} + \bar{p}\right]\cdot\ln\frac{B\bar{f}_{co}+\bar{p}}{I_0}, & L < 0 \end{cases} \tag{19}$$

Correspondingly, the transition condition becomes

$$L = \tau\bar{q} - \left[A + \tan\phi_c(\kappa_c)\right]\cdot\left[B\bar{f}_{co} + \bar{p}\right] \tag{20}$$

where τ adopts the form adapted from the William–Warnke yield function [32], expressed as:

$$\tau = \frac{4\left(1-\varrho^2\right)\cos^2\theta + (2\varrho-1)^2}{2\left(1-\varrho^2\right)\cos\theta + (2\varrho-1)\sqrt{4\left(1-\varrho^2\right)\cos^2\theta + 5\varrho^2 - 4\varrho}} \tag{21}$$

where ϱ controls the evolution of the deviatoric shape.

Generally, the deviatoric trace of the potential surface can be characterized by the normalized polar length $K^G = \bar{q}^G_{TM}/\bar{q}^G_{CM}$, where $\bar{q}^G_{TM}$ and $\bar{q}^G_{CM}$ represent the polar lengths along the tensile and compressive meridians, respectively. By substituting Eq. (21) into Eq. (19) and calculating $\bar{q}^G_{TM}$ and $\bar{q}^G_{CM}$ respectively, the ratio of $\bar{q}^G_{TM}$ to $\bar{q}^G_{CM}$ leads to $K^G = \varrho$. Based on experimental observations, Zheng and Teng [10] suggested that the deviatoric trace should evolve from a circular to a triangular shape. In their model, this evolution is controlled by an assumed evolution function for ϱ that depends

on the internal state variables and can be calibrated via trial-and-error against test data. Nevertheless, calibrating the evolution of ϱ remains relatively complex following the empirical approach adopted by Zheng and Teng [10]. Given similar evolution tendencies of deviatoric traces of the potential and yield surfaces, linking the evolution of the deviatoric component of the potential surface to that of the yield surface simplifies the formulation. Early studies [35–37] have reported that a non-associated flow rule can be obtained from an associated rule by relaxing associativity only as necessary, typically for the volumetric component, thus simplifying constitutive modeling while maintaining good accuracy. Following this philosophy, this study associates the deviatoric shape of the potential surface with that of the yield surface, whereas the volumetric component remains unassociated. Specifically, a straightforward assumption is considered: $K^{\mathrm{G}} = K^{\mathrm{F}}$, where the normalized polar length of the deviatoric trace for the potential function equals the yield strength ratio of the yield surface, as illustrated in Fig. 3(b). Thus, the evolution of ϱ is linked to yield function parameter γ via

$$\varrho = \frac{\gamma(\kappa_{\mathrm{c}})+3}{2\gamma(\kappa_{\mathrm{c}})+3} \tag{22}$$

In summary, assuming equivalence between the normalized polar length of the potential surface K^{G} and the yield strength ratio of the yield surface K^{F} significantly simplifies the determination of the deviatoric shape of the potential surface without compromising the general features of the non-associated flow rule. The validity of this assumption is further confirmed in Sections 6.3 and 7, where it yields reasonably accurate predictions of concrete dilation under non-uniform passive confinement.

3.3. Evolution of internal state variables

One key advantage of the CDP model is its separate treatment of tensile and compressive responses, achieved through two independent internal state variables, κ_{t} and κ_{c}, representing the equivalent plastic strains in tension and compression, respectively. The evolution rates of the tensile and compressive internal state variables, denoted as $\dot{\kappa}_{\mathrm{t}}$ and $\dot{\kappa}_{\mathrm{c}}$, are defined as:

$$\dot{\kappa}_{\mathrm{t}} = r\left(\widehat{\bar{\boldsymbol{\sigma}}}\right)\dot{\widehat{\varepsilon}}^{\mathrm{p}}_{\max} \tag{23}$$

$$\dot{\kappa}_{\mathrm{c}} = -\left[1 - r\left(\widehat{\bar{\boldsymbol{\sigma}}}\right)\right]\dot{\widehat{\varepsilon}}^{\mathrm{p}}_{\min} \tag{24}$$

where $\dot{\widehat{\varepsilon}}^{\mathrm{p}}_{\max}$ and $\dot{\widehat{\varepsilon}}^{\mathrm{p}}_{\min}$ are the algebraic maximum and minimum principal plastic strain rates, respectively; and $r\left(\widehat{\bar{\boldsymbol{\sigma}}}\right)$ is a stress-dependent weight factor defined as:

$$r\left(\widehat{\bar{\boldsymbol{\sigma}}}\right) = \frac{\sum_{i=1}^{3}\left\langle\widehat{\bar{\sigma}}_i\right\rangle}{\sum_{i=1}^{3}\left|\widehat{\bar{\sigma}}_i\right|} \tag{25}$$

where $\widehat{\bar{\sigma}}_i$ is the ith principal effective stress.

Under uniaxial tension or compression, κ_{t} and κ_{c} are equal to the magnitudes of the axial tensile and compressive plastic strains, respectively. Notably, Eq. (24) does not reflect the influence of confinement on the evolution of κ_{c}, leading to identical κ_{c} predictions for axially compressed concrete with and without confinement, a result inconsistent with experimental evidence. As indicated in Section S1, axial strain in the transition state increases substantially (in terms of its magnitude) under confining pressure. Since this discrepancy pertains specifically to the compressive regime, the evolution for κ_{c} requires modification.

One effective way to account for this enhancement in deformation capability involves scaling κ_{c} by a ductility measure χ_{p}. Therefore, Eq. (24) is modified, as adopted by Farahmandpour et al. [28], Grassl et al. [16], and Zheng and Teng [10].

$$\dot{\kappa}_{\mathrm{c}} = -\left[1 - r\left(\widehat{\bar{\boldsymbol{\sigma}}}\right)\right]\frac{\dot{\widehat{\varepsilon}}^{\mathrm{p}}_{\min}}{\chi_{\mathrm{p}}} \tag{26}$$

where χ_{p} denotes a function of the confinement level. To maintain its relevance under complex stress states (such as non-uniform confinement or tension), the confinement level can be expressed using a stress invariant. Following Zheng and Teng [10], the confinement measure η is defined as:

$$\eta = \frac{\langle p/\tau^m - f_{\mathrm{co}}/3\rangle}{f_{\mathrm{co}}} \tag{27}$$

To account for the reduced confinement effect under non-uniform confinement, the term p/τ^m is introduced in Eq. (27), where the deviatoric shape function τ, derived from the potential function, accounts for confinement reduction caused by stress non-uniformity, while the exponent m controls the degree of reduction, as discussed in Section 4.2. According to Zheng and Teng [10], confinement measure η for confined concrete increases until it reaches a transition state. Beyond this state, η decreases under active confinement but continues to increase under passive confinement. This characteristic helps identify passive confinement conditions. In Eq. (27), the hydrostatic pressure in nominal stress space, $p = (1-d)\bar{p}$, is used because damage must be included to reflect the decrease in η due to post-transition softening of actively confined concrete. Conversely, when η is computed in the effective stress space, it continues to increase for both active and passive confinement, making the two situations indistinguishable.

Following a method similar to that adopted by Zheng and Teng [10], the effects of confinement (quantitatively characterized by η) on ductility measure χ_{p} can be quantified by considering axial strain enhancement due to confinement at the transition state (Section S5 in Appendix A), which yields

$$\chi_{\mathrm{p}} = 1 + \left[k_{\mathrm{e}}k_{\mathrm{s}} + \frac{\varepsilon_{\mathrm{c}}^{\mathrm{e,k}}}{\varepsilon_{\mathrm{c}}^{\mathrm{p,k}}}(k_{\mathrm{e}}-1)k_{\mathrm{s}}\right]\cdot\frac{3(1-\alpha)}{3+\gamma}\cdot\eta \tag{28}$$

where $\varepsilon_{\mathrm{c}}^{\mathrm{e,k}}/\varepsilon_{\mathrm{c}}^{\mathrm{p,k}}$ is the ratio of axial elastic to plastic strain in uniaxially compressed concrete at the transition state, and k_{e} is the strain enhancement coefficient (Section S1).

The explicit function between χ_{p} and η exists only with the linear-form yield function used in this study. Conversely, Zheng and Teng [10] recalibrated this relationship using a polynomial expression due to the implicit nature of their equations, considering the confinement effects on ductility.

Using Eqs. (23) and (26), along with the flow rule in Eq. (11), the evolution of the internal state variables can be derived as $\dot{\boldsymbol{\kappa}} = \dot{\lambda}\boldsymbol{H}\left(\bar{\boldsymbol{\sigma}}, \boldsymbol{\kappa}\right)$, where $\dot{\boldsymbol{\kappa}} = [\dot{\kappa}_{\mathrm{t}}, \dot{\kappa}_{\mathrm{c}}]^{\mathrm{T}}$ denotes the evolution rate of the internal state variable vector $\boldsymbol{\kappa} = [\kappa_{\mathrm{t}}, \kappa_{\mathrm{c}}]^{\mathrm{T}}$. Further, $\boldsymbol{H}$ represents the evolution function for the internal state variables, expressed as

$$\boldsymbol{H} = \begin{bmatrix} r\left(\hat{\bar{\boldsymbol{\sigma}}}\right)\dfrac{\partial G}{\partial \hat{\bar{\sigma}}_{\max}} \\ -\dfrac{1 - r\left(\hat{\bar{\boldsymbol{\sigma}}}\right)}{\chi_{\mathrm{p}}}\cdot\dfrac{\partial G}{\partial \hat{\bar{\sigma}}_{\min}} \end{bmatrix} \tag{29}$$

3.4. Hardening and damage functions

According to the strain equivalence hypothesis [38], the strain under nominal stress in a damaged material is equal to that under effective stress in an undamaged material. Therefore, the effective hardening variables $\bar{c}_{\mathrm{t}}$ and $\bar{c}_{\mathrm{c}}$ can be expressed in terms of the

nominal hardening variables c_t and c_c and the damage variables d_t and d_c as:

$$\bar{c}_t(\kappa_t) = \frac{c_t(\kappa_t)}{1-d_t(\kappa_t)} \tag{30}$$

$$\bar{c}_c(\kappa_c) = \frac{c_c(\kappa_c)}{1-d_c(\kappa_c)} \tag{31}$$

Under uniaxial loading, c_t and c_c correspond in magnitude to the axial tensile and compressive stresses, respectively, while the internal state variables κ_t and κ_c reduce to the axial tensile and compressive plastic strains, respectively. The tensile and compressive hardening functions can be derived from the axial stress–strain curves obtained from uniaxial tension and compression tests or from established uniaxial stress–strain models.

The damage functions during tension and compression, $d_t(\kappa_t)$ and $d_c(\kappa_c)$, depict the evolution of tensile and compressive damage variables with their respective internal state variables. Similar to the hardening variables, the evolution of d_t with κ_t and that of d_c with κ_c can be calibrated using stiffness degradation data from uniaxial cyclic tension and compression tests, or from an appropriate theoretical model.

The scalar damage variable d is a generalization of d_t and d_c, and can be expressed as:

$$1 - d = (1 - s_t d_c)(1 - s_c d_t) \tag{32}$$

where s_t and s_c represent the stiffness recovery effects during the tensile and compressive stress reversals, respectively.

$$s_t = 1 - w_t r\left(\hat{\boldsymbol{\sigma}}\right) \tag{33}$$

$$s_c = 1 - w_c\left[1 - r\left(\hat{\boldsymbol{\sigma}}\right)\right] \tag{34}$$

where w_t and w_c are the weight factors that control the degrees of tensile and compressive stiffness recovery, respectively, upon load reversal. According to experimental observations, the compressive stiffness can be fully recovered owing to crack closure when the loading changes from tension to compression, whereas the tensile stiffness cannot be recovered during compression-to-tension reversal upon the development of crushing microcracks. This behavior, represented by $w_t = 0$ and $w_c = 1$, is the default setup in ABAQUS and has been directly adopted in the proposed model.

Since d depends on κ_t and κ_c, the suppression of stiffness degradation due to confinement can be naturally achieved through the evolution of κ_c. According to Eq. (26), the increment in κ_c reduces with the presence of confinement. Consequently, for two axially compressed concrete cylinders with and without confinement, the value of κ_c for the confined concrete is smaller, resulting in a smaller damage variable and thus suppressed stiffness degradation.

4. Calibration of main parameters for the proposed model

As aforementioned, several key parameters of the proposed model require calibration using test data and fall into two categories: parameters related to unconfined concrete and those related to confinement. Unconfined concrete parameters are largely consistent with those in the original CDP model, including elasticity and strength-related material properties, and the evolution of hardening and damage variables. Additionally, the evolution of the dilation angle parameter require calibration. Confinement-related parameters account for confinement effects and should therefore be calibrated using confined concrete test data.

4.1. Calibration of unconfined concrete parameters

4.1.1. Elasticity and strength-related parameters

The elastic modulus E_c, Poisson's ratio ν and compressive cylinder strength f_{co} of the unconfined concrete can be determined through uniaxial compression tests. If test values are unavailable, ν can be selected between 0.18 and 0.20, and E_c can be estimated using the empirical expression $E_c = 4730\sqrt{f_{co}}$ provided in the ACI code [39]. Other strength parameters, such as the uniaxial tensile strength f_{to} and equal-biaxial compressive strength f_{bo} can be computed directly from the tests. In the absence of test data, f_{to} can be approximated as $0.1f_{co}$, and the strength ratio $k_b = f_{bo}/f_{co}$ can be estimated using the empirical formula $k_b = 1.5f_{co}^{-0.075}$ [15].

4.1.2. Evolution of compressive hardening and damage variables

A widely adopted assumption [40] states that $b_c = \varepsilon_c^p/\varepsilon_c^{in}$, the ratio of compressive plastic strain to compressive inelastic strain, remains constant, providing a reasonable balance between accuracy and simplicity. Based on this assumption and using Eq. (31), the evolution of d_c with κ_c can be expressed as

$$d_c(\kappa_c) = 1 - \frac{c_c(\kappa_c)/E_c}{\kappa_c(1/b_c-1)+c_c(\kappa_c)/E_c} \tag{35}$$

Following the recommendation of Birtel and Mark [40], $b_c = 0.7$ is adopted. The evolution of c_c with κ_c can be calibrated using uniaxial compression test data or uniaxial stress–strain models, as discussed in Section 3.4. In this study, the relationship between c_c and κ_c is described by a function with an ascending branch from Grassl et al. [16] and a descending branch from Zheng and Teng [10] as:

$$c_c(\kappa_c) = \begin{cases} \sigma_{c0} + (f_{co} - \sigma_{c0})\left[\left(\frac{\kappa_c}{\varepsilon_c^{p,k}}\right)^3 - 3\left(\frac{\kappa_c}{\varepsilon_c^{p,k}}\right)^2 + 3\left(\frac{\kappa_c}{\varepsilon_c^{p,k}}\right)\right], & \kappa_c \le \varepsilon_c^{p,k} \\ f_{co}\left[1 + \left(\frac{\kappa_c - \varepsilon_c^{p,k}}{\mu_s \varepsilon_c^{p,k}}\right)^{1.5}\right]^{-1.5}, & \kappa_c > \varepsilon_c^{p,k} \end{cases} \tag{36}$$

where the initial compressive yield stress σ_{c0}, the plastic strain at the transition state $\varepsilon_c^{p,k}$, and the softening coefficient μ_s require calibration.

Owing to the constraints expressed in Eq. (10), σ_{c0} exhibits a minimum value ensuring $\gamma \ge 0$, which is directly adopted in this study. Alternatively, an empirical formula such as that from Papanikolaou and Kappos [15], $\sigma_{c0} = f_{co}^{1.855}/60$, can be used. $\varepsilon_c^{p,k}$ is calculated as $\varepsilon_c^{p,k} = b_c(\varepsilon_c^k - f_{co}/E_c)$, where ε_c^k is the axial strain of unconfined concrete under uniaxial compression at the transition state, and μ_s governs the shape of the descending branch. Owing to the brittle nature of concrete compressive failure, scatter exists in the descending branch of the stress–strain curve, making accurate prediction of this phase difficult. Therefore, calibration of μ_s using uniaxial compression test data is recommended. As shown in Section 6, μ_s generally falls between 6 and 14. In the absence of test data, a default value of $\mu_s = 8$ can be adopted.

4.1.3. Evolution of tensile hardening and damage variables

Similar to d_c, the tensile damage variable d_t can be determined using $b_t = \varepsilon_t^p/\varepsilon_t^{in}$, the ratio of tensile plastic strain to tensile inelastic strain, yielding

$$d_t(\kappa_t) = 1 - \frac{c_t(\kappa_t)/E_c}{\kappa_t(1/b_t-1)+c_t(\kappa_t)/E_c} \tag{37}$$

A value of $b_t = 0.1$ can be used as suggested by Birtel and Mark [40]. For members under flexural or eccentric compression with large eccentricity and the possibility of concrete cracking in tension, $b_t = 0$, as proposed by Chen et al. [41], ensures a reasonable prediction of the flexural cracking behavior. When the stress state

is compression-dominant, as in axial compression or compression with limited eccentricity (the focus of this study), b_t = 1 and $d_t = 0$ from Eq. (37), thereby simplifying the formulation without a reduction in accuracy.

The evolution of c_t with κ_t can be calibrated through uniaxial tension tests or uniaxial stress-strain models, as outlined in Section 3.4. To address the non-local behavior, a tensile stress–crack opening width relationship is adopted instead of a constant tensile stress–strain relationship. Following Chen et al. [41], the equation derived by Hordijk [42] is used to express the evolution of the tensile hardening variable as:

$$\frac{c_t(W)}{f_{to}} = \left[1 + \left(a_1 \frac{W}{W_{cr}}\right)^3\right] \exp\left(-a_2 \frac{W}{W_{cr}}\right) - \frac{W}{W_{cr}}\left(1 + a_1^3\right) \exp\left(-a_2\right) \tag{38}$$

where the constants $a_1 = 3.0$ and $a_2 = 6.93$; the crack opening width W is obtained through the element integration of κ_t according to the crack band model [43] to minimize mesh-dependency. For an element with one integration point, the integration is approximated as $W = \kappa_t l_e$, where l_e is the characteristic element length, typically taken as the cubic root of the element volume [29]. The maximum cracking width W_{cr} in Eq. (38) can be estimated using $W_{cr} = 5.14Q/f_{to}$, where Q is the fracture energy required to completely open a unit area of a crack. Following CEB-FIP [44], Q can be estimated from the maximum aggregate size of concrete g as:

$$Q = \left(0.0469g^2 - 0.5g + 26\right)\left(\frac{f_{co}}{10}\right)^{0.7} \tag{39}$$

When test data are unavailable, g = 20 mm according to Chen et al. [41].

4.1.4. Evolution of the plastic Poisson's ratio

For unconfined concrete under uniaxial compression, volumetric behavior transitions from initial compaction to later expansion, as discussed in Section S1, indicating that the dilation angle varies from negative to positive. According to Eq. (S17) in Section S4, ϕ_c is related to the plastic Poisson's ratio ψ, which is defined as the negative ratio of the lateral plastic strain rate ($\dot{\varepsilon}_l^p$) to axial plastic strain rate ($\dot{\varepsilon}_c^p$) (i.e., $\psi = -\dot{\varepsilon}_l^p/\dot{\varepsilon}_c^p$). Due to limitations of the tensile portion of the potential surface and the need for a smooth transition between tensile and compression regions for numerical stability, the initial dilation angle must satisfy $\phi_c > 0^\circ$ (Fig. 3(a)), equivalent to an initial plastic Poisson's ratio of $\psi_0 > 0.5$. However, experimental observations (Section S1) typically demonstrate initial volumetric compaction ($\psi_0 < 0.5$). To resolve the Gordian knot, the proposed model estimates plastic volumetric change using a slight expansion corresponding to $\psi_0 > 0.5$ (such as $\psi_0 = 0.51$). Although this approximation leads to a slightly overestimated expansion in the early plastic stage, its influence on the prediction of full-range behavior is negligible, as discussed in Section 6.

In the proposed model, the variation of ψ with κ_c is represented as:

$$\psi = \begin{cases} \psi_0 + (\psi_k - \psi_0)\left(\frac{\kappa_c}{\varepsilon_c^{p,k}}\right)^h, & \kappa_c \le \varepsilon_c^{p,k} \\ \psi_k + h(\psi_k - \psi_0)\left(\frac{\kappa_c - \varepsilon_c^{p,k}}{\varepsilon_c^{p,k}}\right), & \kappa_c > \varepsilon_c^{p,k} \end{cases} \tag{40}$$

The evolution of ψ is determined by the plastic Poisson's ratio at the transition state ψ_k and the exponent h that controls the slope of the second branch of the evolution function. The value of ψ_k can be calibrated using the plastic volumetric strain ε_v^p as:

$$\varepsilon_v^p = \int_0^{\varepsilon_c^{p,k}} [2\psi(\kappa_c) - 1]\dot{\kappa}_c \tag{41}$$

Substituting Eq. (40) into Eq. (41) leads to

$$\psi_k = \frac{h+1}{2}\left(1 + \frac{\varepsilon_v^p}{\varepsilon_c^{p,k}}\right) - h\psi_0 \tag{42}$$

where ε_v^p is expressed as $\varepsilon_v^p = \varepsilon_v - \varepsilon_v^e$. The elastic volumetric strain $\varepsilon_v^e = -(1-2\upsilon)\bar{f}_{co}/E_c$ and $\bar{f}_{co} = f_{co} + (1-b_c)(\varepsilon_c^k E_c - f_{co})$. The exponent h determines the rate of dilation and should be calibrated by matching the predicted axial–lateral strain curve with the test curve. In this study, h lies between 1 and 3 and provides predictions in reasonable agreement with the experimental results, as described in Section 6.

4.2. Calibration of confinement-related parameters

According to Eqs. (S1) and (S2) in Section S1, k_s and k_e can be calibrated through compression tests of the actively confined concrete, as:

$$k_s = \frac{f_{cc}^* - f_{co}}{\sigma_l} \tag{43}$$

$$k_e = \frac{\varepsilon_{cc}^{k,*}/\varepsilon_c^k - 1}{f_{cc}^*/f_{co} - 1} \tag{44}$$

where f_{cc}^* and $\varepsilon_{cc}^{k,*}$ denote axial compressive strength and corresponding axial strain; and σ_l is the confining pressure. If test data are unavailable, default values of $k_s = 3.5$ and $k_e = 5.0$ can be used, as suggested by Teng et al. [7].

The exponent m, controlling confinement reduction, is calibrated through an equal-biaxial compression test, where the stress state lies on the tensile meridian ($\theta = 0^\circ$) and represents the highest degree of non-uniformity. Due to symmetry, the deviatoric component of the predicted flow direction should align with the tensile meridian (Fig. 3); thus, deformation prediction depends solely on m and is unaffected by the evolution of the deviatoric trace of the potential surface. Based on a trial-and-error procedure, $m = 2$ offers the best match for the test curves.

As the plastic dilation tendency of actively confined concrete resembles that of unconfined concrete, it can be predicted using an appropriately designed potential surface, as described in Section 3.2.1. However, for passively confined concrete, the dilation behavior differs markedly, exhibiting an inflection in the axial–lateral strain curve [45], as introduced in Section S1. This inflection implies that the plastic Poisson's ratio begins to decrease after an initial increase, thus requiring an additional reduction term to account for the influence of passive confinement. As discussed in Section 3.4, the positive rate of confinement measure ($\dot{\eta} > 0$) after the transition state indicates passive confinement. Therefore, reduced plastic Poisson's ratio ψ_r can be expressed as:

$$\psi_r(\kappa_c) = \psi_c(\kappa_c)\frac{1}{2}\left(\frac{1}{\sqrt{1+12.5\left\langle\int\dot{\eta}\right\rangle}} + \frac{1}{\exp\left(16\left\langle\int\dot{\eta}\right\rangle\right)}\right) \tag{45}$$

where the reduction of ψ_r increases with the accumulation of confinement measures.

5. Numerical implementation in explicit analysis

A summary of the governing equations for the proposed model is provided in Section S6 in Appendix A to facilitate numerical implementation. In ABAQUS, an explicit dynamic solver based on the central difference method [46] is used to resolve the nonlinear global force–displacement relationship. This explicit approach avoids convergence issues when simulating complex structures such as eccentrically compressed FCC columns. To maintain

quasistatic conditions, global kinematic energy is conserved below 10% of the internal energy [29]. For this study, the proposed model was implemented in ABAQUS through the user-defined material subroutine VUMAT for explicit solver, which defines a nonlinear stress–strain relationship at element integration points. As stresses at the integration points must be integrated to obtain internal forces, VUMAT adopts an implicit method to ensure accuracy and avoid error accumulation [47]. Consequently, an elastic trial-plastic return method [17] was used to solve implicit equations governing nonlinear stress–strain response at each integration point. A flowchart and detailed numerical procedure for this algorithm are provided in Section S7 in Appendix A.

The proposed model presents greater convergence challenges than the original CDP model owing to more complex formulations. The convergence of the Newton–Raphson method depends strongly on the initial stress guess provided by the elastic predictor. When the elastic trial stress deviates significantly from the true solution, required iterations increase substantially or lead to divergence. When divergence occurs, the current strain increment $\Delta\boldsymbol{\varepsilon}$ is subdivided into smaller sub-increments; the current step is replaced by multiple sub-steps with reduced step sizes. This subdivision generally improves convergence but increases computational time.

6. Model verification against confined concrete under different loading conditions

This section validates the proposed model against confined concrete under different loading conditions, focusing on the stress–strain responses. Following Zheng and Teng [10], the confined concrete was modeled in ABAQUS using a single 8-node three-dimensional solid element with reduced integration (C3D8R). Throughout this study, an element size of 10 mm was considered; however, the numerical results remained mesh-independent owing to the simulated homogeneous stress–strain states.

Unless otherwise specified, the model parameters were determined using the calibration procedures outlined in Section 4. The original CDP model, which forms the basis of this study, was used for comparison to highlight improvements in the proposed model. As discussed in Section 4, the CDP model shared several parameters with the proposed model, excluding two parameters: K^{F} and ϕ, which varied in the proposed model but remained constant in the original CDP model. The constant ratio K^{F} exhibited the value used in the proposed model at the transition state. The constant dilation angle ϕ was determined through trial-and-error to best match the lateral–axial strain curve of unconfined concrete, subjected to an upper limit of 56.3° [29].

6.1. Monotonic and cyclic compression of concrete under uniform active confinement

The proposed model was first validated against monotonic compression tests of actively confined concrete reported by Lim and Ozbakkaloglu [13]. The specimen details and model parameters are presented in Table 2 [13,48,49]. As shown in Fig. 4(a) [13], although the CDP model accurately predicted axial strength, it significantly underestimated axial strain. By incorporating a ductility measure into the internal state variable evolution (Section 3.4), the proposed model predicted axial strain more accurately, aligning with the test axial stress–strain curves. Additionally, comparisons of the lateral–axial strain and axial stress–volumetric strain curves (Fig. 4 [13]) confirmed that the CDP model could not adequately capture concrete dilation, whereas the proposed meridian trace of the potential surface accurately predicted variations in the plastic Poisson's ratio and volumetric changes under different confining pressures.

The capability of the proposed model to predict stiffness degradation under active confinement was verified against the test data reported by Imran [48] and Imran and Pantazopoulou [49]. Specimens were numbered following the format used by Lim and Ozbakkaloglu [13] because the original paper did not provide specimen identifiers (ID). The specimen details and model parameters are listed in Table 2 [13,48,49]. For unconfined concrete, the CDP and proposed models consistently predicted axial stress–strain curves (Fig. 5(a) [48,49]), as they shared the same hardening function. However, the CDP model underestimated volumetric expansion (Fig. 5(b) [48,49]) even with the maximum allowable value of ϕ. By contrast, the proposed evolution function for the plastic Poisson's ratio (Section 4.1.4) exhibited good agreement with the test results. As shown in Figs. 5(c)–(e) [48,49], the CDP model exhibited shortcomings similar to those aforementioned. Furthermore, the model underestimated unloading stiffness, indicating its inability to capture the suppression of stiffness degradation owing to confinement. Conversely, the proposed model aligned with the test results. Degraded stiffness during unloading agreed well under different confinement levels and captured the lower stiffness degradation under higher confining pressure. Comparisons (Fig. 5 [48,49]) established that damage evolution and modified evolution laws for internal state variables accurately represented stiffness degradation under confinement.

To quantitatively assess the accuracy of the proposed model in predicting actively confined concrete, key results, including the axial compressive strength f_{cc}^{*} and the corresponding axial strain $\varepsilon_{\mathrm{cc}}^{\mathrm{k},*}$, were compared with test data, as summarized in Table 3 [13,48,49]. The model accurately predicted f_{cc}^{*}, with a maximum error below 10%. Larger errors occurred for $\varepsilon_{\mathrm{cc}}^{\mathrm{k},*}$, although values remained within 25%. Since the axial stress–strain curves exhibited a stress plateau, slight fluctuations in test curves generated significant variations in $\varepsilon_{\mathrm{cc}}^{\mathrm{k},*}$. These discrepancies were acceptable because the proposed model captured the overall response trends, as shown in Figs. 4 [13] and 5 [48,49].

6.2. Monotonic and cyclic compression of concrete under uniform passive confinement

For passively confined concrete, the proposed model was verified using the test results reported by Lim and Ozbakkaloglu [13]. Passively confined cylindrical concrete specimens exhibited the same dimensions and concrete batches as their actively confined counterparts. The FRP confinement is quantified using a confinement stiffness K_{FRP} defined as $2E_{\mathrm{f}}t_{\mathrm{f}}/D_{\mathrm{f}}$, where E_{f} and t_{f} are the hoop elastic modulus and thickness of the FRP, respectively, and D_{f} is the diameter of the specimen cross-section. The passively confined specimens fail when FRP reaches hoop rupture strain $\varepsilon_{\mathrm{h,rup}}$. The model parameters used to simulate these specimens matched those presented in Table 2 [13,48,49], excluding k_{s}, which was taken as the weighted average from active confinement: $k_{\mathrm{s}} = \left(\sum_{i=1}^{4} k_{si}\sigma_{\mathrm{li}}\right)/\left(\sum_{i=1}^{4}\sigma_{\mathrm{li}}\right)$, where k_{si} refers to the confinement effectiveness coefficient obtained under the corresponding confining pressure σ_{li}. The specimen details and model parameters are listed in Table 4 [13,45,50]. As shown in Fig. 6(a) [13], the CDP model underestimated the stiffness of the ascending branch after the transition state owing to limitations in yield and potential functions. From the lateral–axial strain curves (Fig. 6(a) [13]) and axial stress–volumetric strain curves (Fig. 6(b) [13]), the CDP model overestimated concrete dilation early in loading but underestimated it later. Conversely, the proposed model exhibiting unique modifications predicted dilation more accurately. Furthermore, the model accurately captured the stiffness of the second

Table 2
Actively confined concrete: specimen details and model parameters.

Reference	Loading scheme	Specimen	Specimen information					Proposed model parameter					CDP model parameter	
			f_{co} (MPa)	ε_c^k(%)	E_c (MPa)	v	σ_l(MPa)	μ_s	ψ_k	h	k_s	k_e	K^F	ϕ(°)
Lim and Ozbakkaloglu [13]	Monotonic	N52-T0	51.6	0.220	–	–	0	8.0	1.0	3	–	–	0.68	56
		N52-T5	51.6	0.220	–	–	5.0	8.0	1.0	3	4.80	5.0	0.66	56
		N52-T10	51.6	0.220	–	–	10.0	8.0	1.0	3	4.34	5.0	0.68	56
		N52-T15	51.6	0.220	–	–	15.0	8.0	1.0	3	4.23	5.0	0.68	56
		N52-T25	51.6	0.220	–	–	25.0	8.0	1.0	3	3.90	5.0	0.70	56
Imran [48]; Imran and Pantazopoulou [49]	Cyclic	N28-T0	28.6	0.260	21 250	0.21	0	6.0	1.8	1	–	–	0.68	56
		N28-T4	28.6	0.260	21 250	0.21	4.2	6.0	1.8	1	5.05	5.0	0.66	56
		N28-T8	28.6	0.260	21 250	0.21	8.4	6.0	1.8	1	4.46	5.0	0.68	56
		N28-T14	28.6	0.260	21 250	0.21	14.7	6.0	1.8	1	4.44	5.0	0.68	56

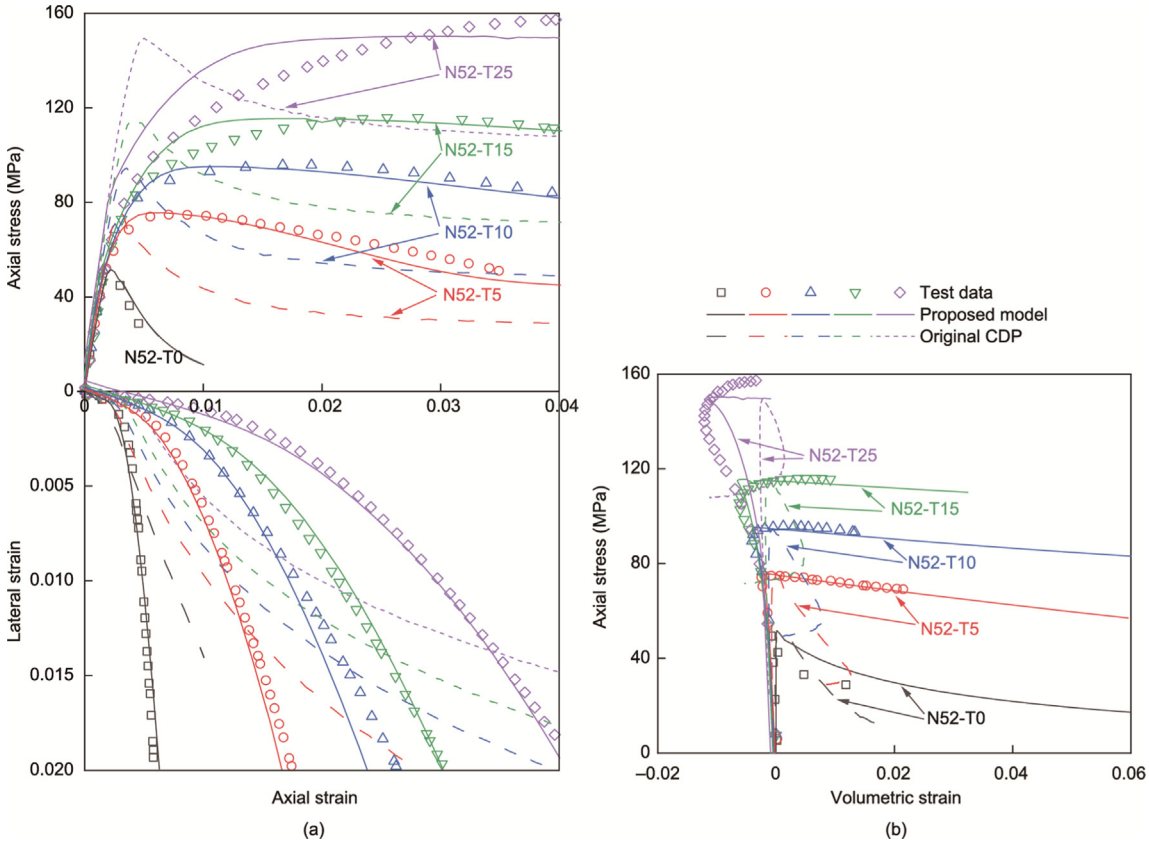

Fig. 4. Predicted versus test results for actively confined concrete under monotonic compression [13]: (a) axial stress–strain and axial–lateral strain curve; and (b) axial stress–volumetric strain curve.

branch of the axial stress–strain curve, although dilation prediction showed less agreement with the test lateral–axial strain and axial stress–volumetric strain curves. As dilation under the largest confinement stiffness was accurately captured (blue line in Fig. 6 [13]), slight discrepancies under lower confinement stiffness were observed from experimental variability because the test curves under different confinement stiffnesses lacked clear trends. Despite these minor disagreements, the proposed model captured inflection in the lateral–axial strain curve and reversal from the volumetric expansion to compaction under increasing confining pressure.

To further demonstrate the capability of the proposed model in handling varying confinement stiffness levels, the model was verified against the test data reported by Jiang and Teng [45]. Three specimen groups representing strong, medium, and weak confinement were selected, each containing two nominally identical specimens, as listed in Table 4 [13,45,50]. As shown in Fig. 7 [45], the CDP model underestimated dilation under weak confinement, even when the maximum allowable ϕ was used. Under medium and strong confinement, the CDP model initially fit the lateral–axial strain curves but later deviated, resulting in an underestimated dilation. Moreover, the CDP model failed to accurately capture axial stress enhancement, even when predicted lateral–axial strain curves aligned reasonably with the test curves. Thus, comparative analysis demonstrated that the proposed model substantially improved the prediction of both strength and deformation behavior of concrete under different confinement stiffnesses, including the descending branch of the stress–strain curve after the transition state caused by insufficient confinement stiffness (or weak confinement).

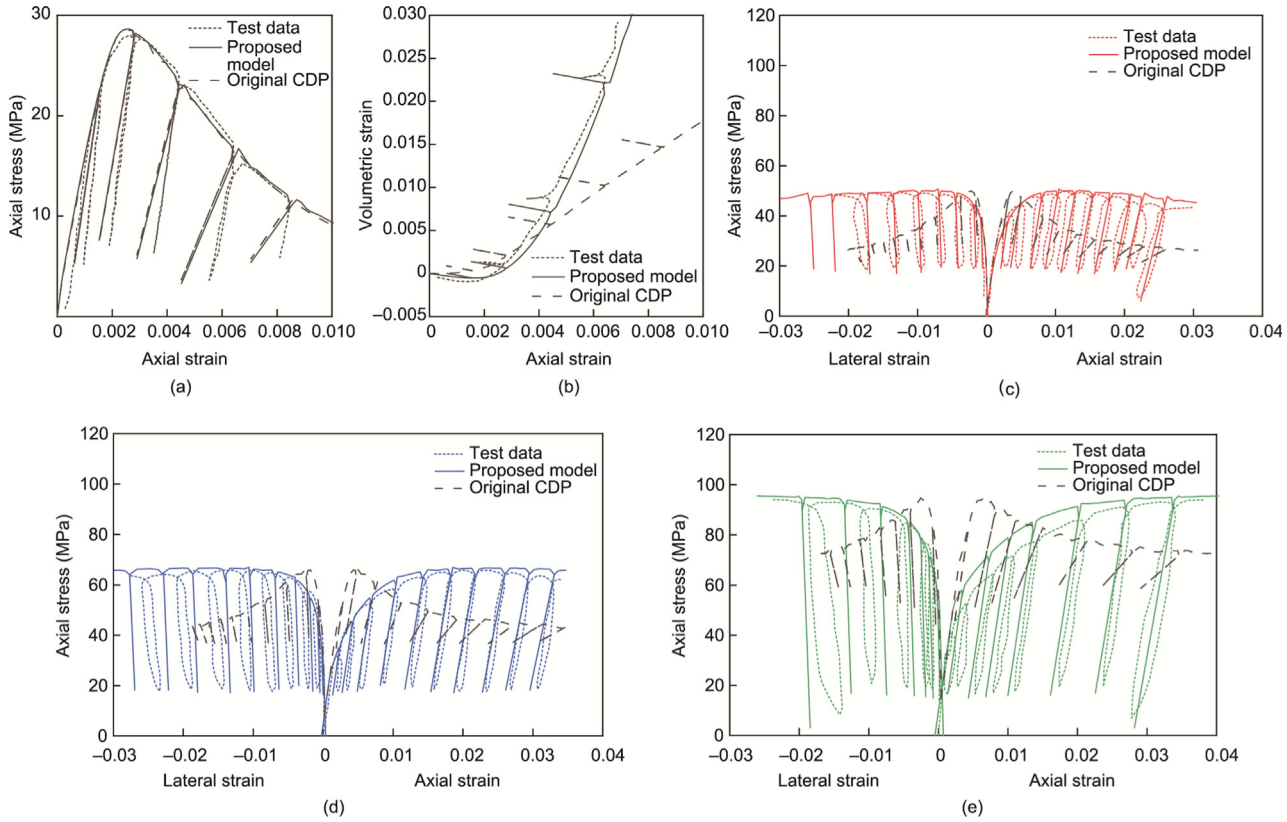

Fig. 5. Predicted versus test results for actively confined concrete under cyclic compression [48,49]: (a) axial stress–strain curve of unconfined specimen N28-T0; (b) volumetric strain–axial strain curve of unconfined specimen N28-T0; (c) stress–strain curve of specimen N28-T4 under confining stress = 4.2 MPa; (d) stress–strain curve of specimen N28-T8 under confining stress = 8.4 MPa; and (e) stress–strain curve of specimen N28-T14 under confining stress = 14.7 MPa.

Table 3
Comparison of key test and predicted results for actively confined concrete specimens.

Reference	Specimen	f^*_{cc}(MPa) (Test)	f^*_{cc}(MPa) (FE)	Error (%)	$\varepsilon^{k,*}_{cc}$(%) (Test)	$\varepsilon^{k,*}_{cc}$ (%) (FE)	Error (%)
Lim and Ozbakkaloglu [13]	N52-T5	73.1	76.0	3.97	0.710	1.020	43.66
	N52-T10	93.2	97.0	4.08	2.023	1.820	−10.03
	N52-T15	114.6	115.4	0.70	2.963	2.460	−16.98
	N52-T25	158.3	148.1	−6.44	4.230	3.740	−11.58
Imran [48]; Imran and Pantazopoulou[49]	N28-T4	48.1	50.7	5.41	1.385	1.051	−24.12
	N28-T8	65.2	67.0	2.76	2.375	1.855	−21.89
	N28-T14	92.3	95.5	3.47	3.425	4.030	17.66

Error (%) = [(FE result − Test result) / Test result] × 100. "Test" represents the test results that are averaged over nominally identical specimens; "FE" denotes finite element results obtained using the proposed model.

Table 4
Passively confined concrete: specimen details and model parameters.

Reference	Loading Scheme	Specimen	Specimen information						Proposed model parameter					CDP model parameter	
			f_{co} (MPa)	ε^k_c(%)	E_c (MPa)	v	K_{FRP} (MPa)	$\varepsilon_{h,rup}$ (%)	μ_s	ψ_k	h	k_s	k_e	K^F	ϕ(°)
Lim and Ozbakkaloglu [13]	Monotonic	N52-G1	51.6	0.220	–	–	605	1.995	8.0	1.0	3	4.15	5.0	0.68	56
		N52-G2	51.6	0.220	–	–	1210	2.293	8.0	1.0	3	4.15	5.0	0.68	56
		N52-C1	51.6	0.220	–	–	830	1.420	8.0	1.0	3	4.15	5.0	0.68	56
		N52-C2	51.6	0.220	–	–	1660	1.570	8.0	1.0	3	4.15	5.0	0.68	56
Jiang and Teng [45]	Monotonic	24/25	39.6	0.263	–	–	538	1.811	8.0	1.3	3	3.5	5.0	0.72	52
		28/29	45.9	0.243	–	–	179	1.719	8.0	1.3	3	3.5	5.0	0.72	56
		34/35	38.0	0.217	–	–	2154	0.971	8.0	1.3	3	3.5	5.0	0.72	40
Lam et al. [50]	Cyclic	CI-SC1	41.1	0.256	–	–	543	1.320	6.0	1.5	3	3.5	5.0	0.72	40
		CII-SC2	38.9	0.250	–	–	1073	1.080	6.0	1.5	3	3.5	5.0	0.72	40

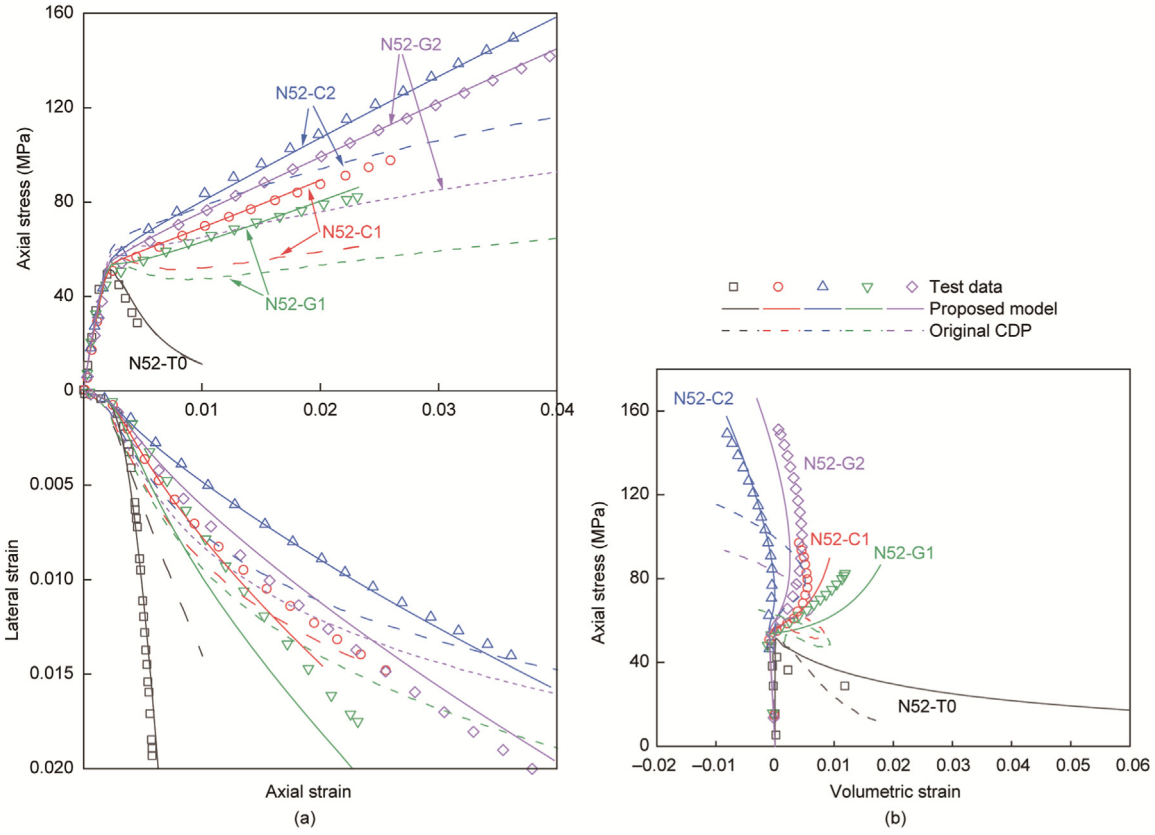

Fig. 6. Predicted versus test results for passively confined concrete under monotonic compression [13]. (a) Axial stress–strain and axial–lateral strain curve; (b) axial stress–volumetric strain curve.

Lam et al. [50] conducted cyclic compression tests on passively confined concrete, and their test results were used to validate the proposed model, particularly its capability to simulate stiffness degradation of confined concrete under cyclic compression. Specimen details and model parameters are listed in Table 4 [13,45,50]. As shown in Fig. 8 [50], excluding the aforementioned shortcomings, the CDP model overestimated stiffness degradation. Conversely, the proposed model, which accounts for confinement effects, exhibited good agreement with test curves, including unloading stiffness.

The ultimate state of the passively confined specimens, characterized by hoop rupture of the FRP, was further examined. The ultimate axial stress f_{cu} and ultimate axial strain ε_{cu} were determined and compared with test data to assess model accuracy. As listed in Table 5 [13,45,50], the errors for f_{cu} and ε_{cu} remained within 10% for most specimens, while the maximum error recorded 15.32% for f_{cu} and −15.79% for ε_{cu}. This close agreement reaffirmed the accuracy and rationality of the proposed model.

6.3. Concrete under non-uniform passive confinement

The proposed model was further validated against tests proposed by Mohammadi and Wu [25], who tested concrete cubes under non-uniform passive confinement using aluminum plates and bolts that allowed independent control of lateral confinement stiffness in the two transverse directions. The ratios of these confinement stiffnesses, denoted as $K^1_{FRP} : K^2_{FRP}$, ranged from $K^1_{FRP} : K^2_{FRP} = 2 : 2$ (uniform confinement) to 2 : 0 (biaxial compression). The specimens were renumbered because the original paper did not provide specimen IDs. Default model parameter values were adopted, except for the softening coefficient μ_s, which was fitted using the axial stress–strain curve under uniform confinement. For the CDP model, $\phi = 56^\circ$ matched lateral strains under uniform confinement. Specimen details and model parameters are listed in Table 6 [25].

As shown in Fig. 9 [25], the CDP model closely predicted the axial stress–strain curves only for the specimen with $K^1_{FRP} : K^2_{FRP} = 2 : 0$, where confinement was significantly weak. For specimens with stronger confinement, the CDP model underestimated axial stress after the transition state. Additionally, the difference between the two predicted lateral strains was significantly smaller than that in the test results, highlighting the limitations of the potential surface of the original CDP model. Conversely, the proposed model accurately captured the strength and deformation behavior under varying confinement non-uniformities. In particular, the model reflected the difference between the two lateral strains across different confinement non-uniformity levels, demonstrating the feasibility of the evolution law for the deviatoric potential trace (Section 3.2.2).

7. Model verification against eccentrically loaded FRP-confined columns

Although the proposed model was verified for confined concrete under simple loading conditions (Section 6), further validation against the eccentric compression tests of FCC specimens reported by Zhang [51] and Jiang et al. [52] was performed to examine the ability of the model in handling complex stress states. FCC specimens replaced CFFT specimens because the FRP–concrete interfacial bond in FCC is significantly stronger, thereby minimizing debonding or slip effects, whereas the FRP–concrete interaction is substantially complex and requires further research.

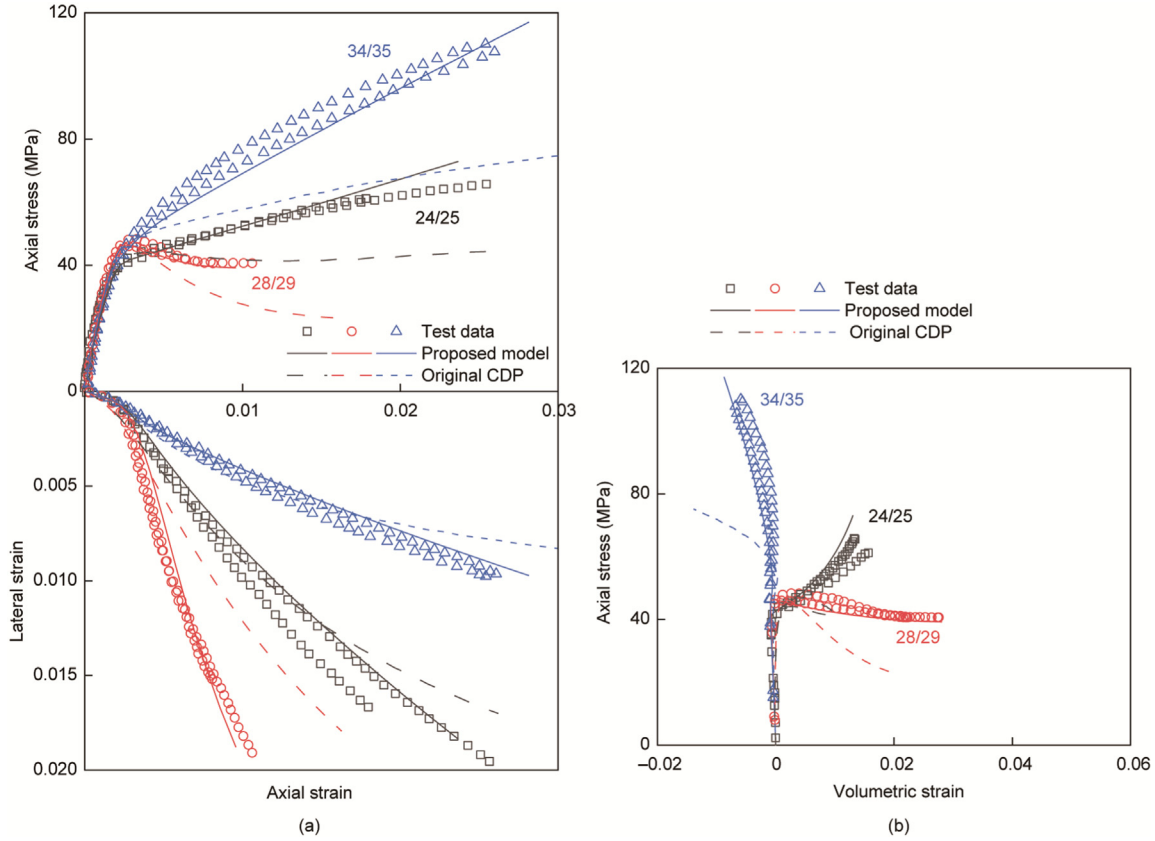

Fig. 7. Predicted versus test results for passively confined concrete under monotonic compression [45]. (a) Axial stress–strain and axial–lateral strain curve; (b) axial stress–volumetric strain curve.

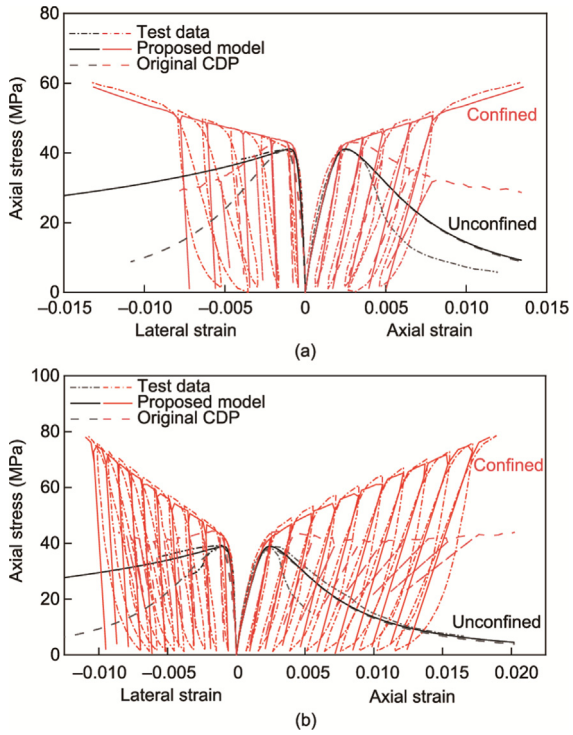

Fig. 8. Predicted versus test results for passively confined concrete under cyclic compression [50]. (a) Stress–strain curve of specimen CI-SC1 with confinement stiffness = 543 MPa; (b) stress–strain curve of specimen CII-SC2 with confinement stiffness = 1073 MPa.

7.1. Test specimens and finite element (FE) modeling

All selected specimens were cylinders measuring 150 mm × 300 mm and confined with 2-ply carbon fiber sheets applied by a wet lay-up process, providing a nominal confinement stiffness K_{FRP} of 782 MPa. The specimens were tested under five load eccentricities (e) ranging from 0 (concentric) to 40 mm, as summarized in Table 7 [51,52]. Two nominally identical specimens were tested at each eccentricity and distinguished by suffixes A and B.

In FE modeling of each specimen, the end plate was modeled as a rigid steel body without deformation. The hinge allowing eccentricity adjustment was modeled through a reference point located at the rotational center of the hinge (20 mm above the specimen end). An eccentric load was applied by imposing a vertical displacement on the reference point while restraining its horizontal motion, causing the rigid plate to move downward and simultaneously rotate about the reference point. As the specimen was encased in the steel endplate, a tie constraint modeled the interface between the endplate and the concrete top surface. The bond between the FRP sheet and concrete was designed as a tie constraint because the wet lay-up process produced a sufficiently strong interface to prevent debonding. To improve computational efficiency, the model included only half of the specimen height by exploiting symmetry. The concrete was modeled using C3D8R elements, whereas the FRP sheet was modeled using 4-node three-dimensional shell elements with reduced integration (S4R). A mesh convergence study (Section S8 in Appendix A) indicated that an average mesh size of 10 mm offered a suitable balance between accuracy and computational cost. A schematic of the resulting FE model is shown in Fig. 10 [51,52].

Table 5
Comparison of key test and predicted results for passively confined concrete specimens.

Reference	Specimen	f_{cu}(MPa) (Test)	f_{cu}(MPa) (FE)	Error (%)	ε_{cu}(%) (Test)	ε_{cu} (%)(FE)	Error (%)
Lim and Ozbakkaloglu [13]	N52-G1	91.5	86.3	−5.68	2.675	2.326	−13.05
	N52-G2	160.4	165.2	2.99	4.663	4.901	5.10
	N52-C1	96.9	89.7	−7.43	2.400	2.021	−15.79
	N52-C2	152.2	158.3	4.01	3.746	3.991	6.54
Jiang and Teng [45]	24/25	63.3	73.0	15.32	2.175	2.369	8.92
	28/29	40.5	39.2	−3.21	0.938	0.957	2.03
	34/35	108.8	117.1	7.63	2.582	2.816	9.06
Lam et al. [50]	CI-SC1	60.2	58.9	−2.16	1.340	1.353	0.97
	CII-SC2	78.2	77.9	−0.38	1.890	1.841	−2.59

Error (%) = [(FE result − Test result) / Test result] × 100. "Test" represents the test results that are averaged over nominally identical specimens; "FE" denotes finite element results obtained using the proposed model.

Table 6
Concrete under non-uniform passive confinement: specimen details and model parameters.

Reference	Loading scheme	Specimen	Specimen information						Proposed model parameter					CDP model parameter	
			f_{co} (MPa)	ε_c^k(%)	E_c (MPa)	v	K^1_{FRP}(MPa)	K^2_{FRP}(MPa)	μ_s	ψ_k	h	k_s	k_e	K^F	ϕ (°)
Mohammadi and Wu [25]	Monotonic	N52.8-2-2	52.8	–	–	–	1080	1080	8.0	1.3	3	3.5	5.0	0.71	56
		N52.8-2-1	52.8	–	–	–	1080	540	8.0	1.3	3	3.5	5.0	0.71	56
		N52.8-2-0.5	52.8	–	–	–	1080	270	8.0	1.3	3	3.5	5.0	0.71	56
		N52.8-2-0	52.8	–	–	–	1080	0	8.0	1.3	3	3.5	5.0	0.71	56

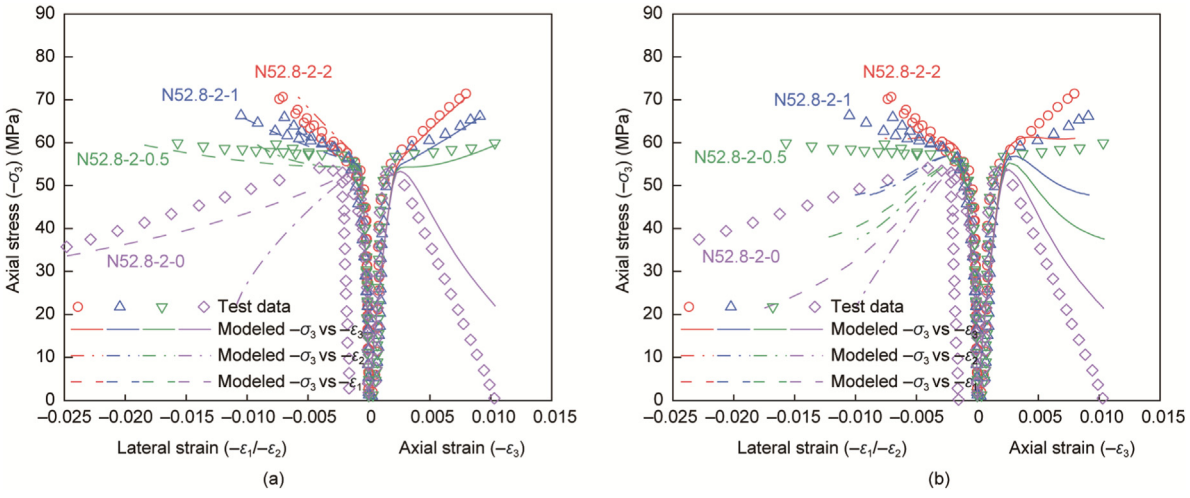

Fig. 9. Predicted versus test results for concrete under non-uniform passive confinement [25]. (a) Predictions by the proposed model; (b) predicitons by the CDP model. vs: versus.

Table 7
FRP-confined concrete under eccentric compression: specimen details and model parameters.

References	Specimen	Specimen information							Proposed model parameter					CDP model parameter	
		f_{co} (MPa)	ε_c^k(%)	E_c (MPa)	v	K_{FRP} (MPa)	$\varepsilon_{h,rup}$ (%)	e (mm)	μ_s	ψ_k	h	k_s	k_e	K^F	ϕ (°)
Zhang [51] and Jiang et al. [52]	L2E0A/B	39.4	0.201	35 807	–	782	1.428	0	14.0	1.0	3	3.5	5.0	0.72	40
	L2E10A/B	39.4	0.201	35 807	–	782	1.428	10	14.0	1.0	3	3.5	5.0	0.72	40
	L2E20A/B	39.4	0.201	35 807	–	782	1.513	20	14.0	1.0	3	3.5	5.0	0.72	40
	L2E30A/B	39.4	0.201	35 807	–	782	1.308	30	14.0	1.0	3	3.5	5.0	0.72	40
	L2E40A/B	39.4	0.201	35 807	–	782	1.123	40	14.0	1.0	3	3.5	5.0	0.72	40

The proposed constitutive model was used to simulate confined concrete behavior. Default model parameter values were adopted, except that the parameters μ_s, ψ_k, and n were calibrated by matching axial load–axial strain and hoop–axial strain curves of the concentrically compressed specimen. For comparison, the original CDP model in ABAQUS was applied, with the constant ϕ set to 40° to match the hoop–axial strain curve of the concentrically compressed specimen. Model parameters are listed in Table 7 [51,52].

Wet lay-up FRP was modeled with the "lamina" option in ABAQUS to represent plane orthotropic elasticity. The model further simplified FRP as a unidirectional elastic material in the hoop direction with negligible elastic stiffness in the axial direction (assigned a value near zero). This simplification was justified because

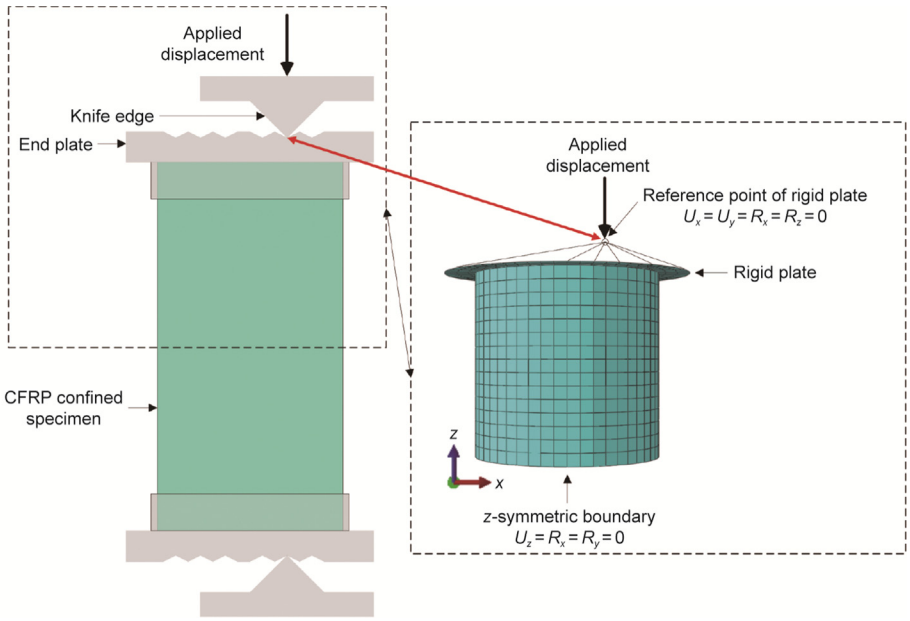

Fig. 10. Finite element model of eccentrically compressed FCC specimen [51,52]. U_x, U_y, and U_z represent displacements in x, y, and z directions, respectively; R_x, R_y, and R_z represent rotations about x, y, and z axes, respectively.

the fibers were oriented in the hoop direction, resulting in a negligible elastic modulus in the axial direction of the specimen. The confinement stiffness and measured hoop rupture strain averaged from the two nominally identical specimens are listed in Table 7 [51,52]. The Hashin damage criterion [53] was used to model FRP damage and failure. Under the unidirectional assumption, the model considered only fiber-direction (hoop) damage. Damage initiation was defined by a fiber tension criterion as $F_f^t = \left(\widehat{\sigma}_{11}/X^T\right)^2$. When the effective tensile stress $\widehat{\sigma}_{11}$ in the fiber direction exceeded tensile strength X^T (i.e., $F_f^t > 1$), the initiation of damage was observed. Thus, X^T was considered as the product of measured hoop rupture strain and hoop elastic modulus. Given the abrupt and brittle nature of FRP fiber rupture, no damage progression was modeled; upon satisfying the initiation criterion, FRP stress and stiffness were immediately reduced to zero. The "element deletion" option in ABAQUS was used to remove the element from the analysis.

7.2. Numerical results

FE analyses revealed that all specimens failed owing to FRP hoop rupture. Typical principal stress profiles at key stages are illustrated in Fig. 11 [51,52]. FRP rupture occurred at the extreme compression fiber (Fig. 11(b)), as element deletion indicated following fiber tension failure. After rupture, FRP stopped exerting confining pressure on the concrete core, causing a sudden stress drop near the rupture zone, as shown in Figs. 11(c) and (d).

The predicted load–deformation responses were validated against test data using load–axial strain (Fig. 12 [51,52]) and load–lateral deflection (Fig. 13 [51,52]) curves. The predicted axial–lateral strain curves at the extreme compression fiber of the mid-height section were extracted and compared with experimental curves, as shown in Fig. 14 [51,52]. The CDP model predicted the response accurately prior to the transition state. Beyond this point, the model underestimated both load and deformation capability. Notably, prediction errors decreased with increasing load eccentricity (Figs. 12(a) and 13(a) [51,52]). Therefore, errors were generated primarily from the inaccurate prediction of compressive strength of passively confined concrete because a larger eccentricity produces a smaller compression zone. Furthermore, the lateral–axial strain relationships predicted by the CDP model deviated from the test response trends in the later loading stage, and the model overestimated lateral strain under larger eccentricities (Fig. 14(a) [51,52]). Conversely, the proposed model addressed the limitations of the original CDP model and accurately predicted global load–deformation behavior (Figs. 12(b) and 13 (b) [51,52]) and lateral–axial strain relationships (Fig. 14(b) [51,52]) of FCC columns across various load eccentricities. As shown in Table 8 [51,52], most predicted load capacities and ultimate deflections exhibited errors within 10%, confirming model accuracy.

To investigate non-uniform concrete dilation, the hoop strain distribution at the mid-height section was extracted from the FE model and compared with the test results, as shown in Fig. 15 [51,52]. The proposed model accurately predicted the hoop strain distribution under different eccentricities. Furthermore, the hoop strain distributions at various loading stages within a single specimen were well captured, thereby validating the feasibility of dilation modeling of the proposed model.

The capability of the proposed model in simulating concrete cracking is illustrated in Fig. 16 [51,52]. As a tie constraint was adopted between the FRP and concrete, crack widths in the two materials were essentially identical. Although a quantitative comparison of the crack widths was not feasible due to the lack of corresponding test measurements, simulated cracking patterns were consistent with experimental observations [51].

8. Conclusions

This study presents a generic damaged-plasticity constitutive model for confined concrete under various stress states, with key advances and findings summarized as follows:

(1) The evolution of the Lubliner–Lee yield surface was modified to improve the prediction of initial yield stress under high confining pressure.

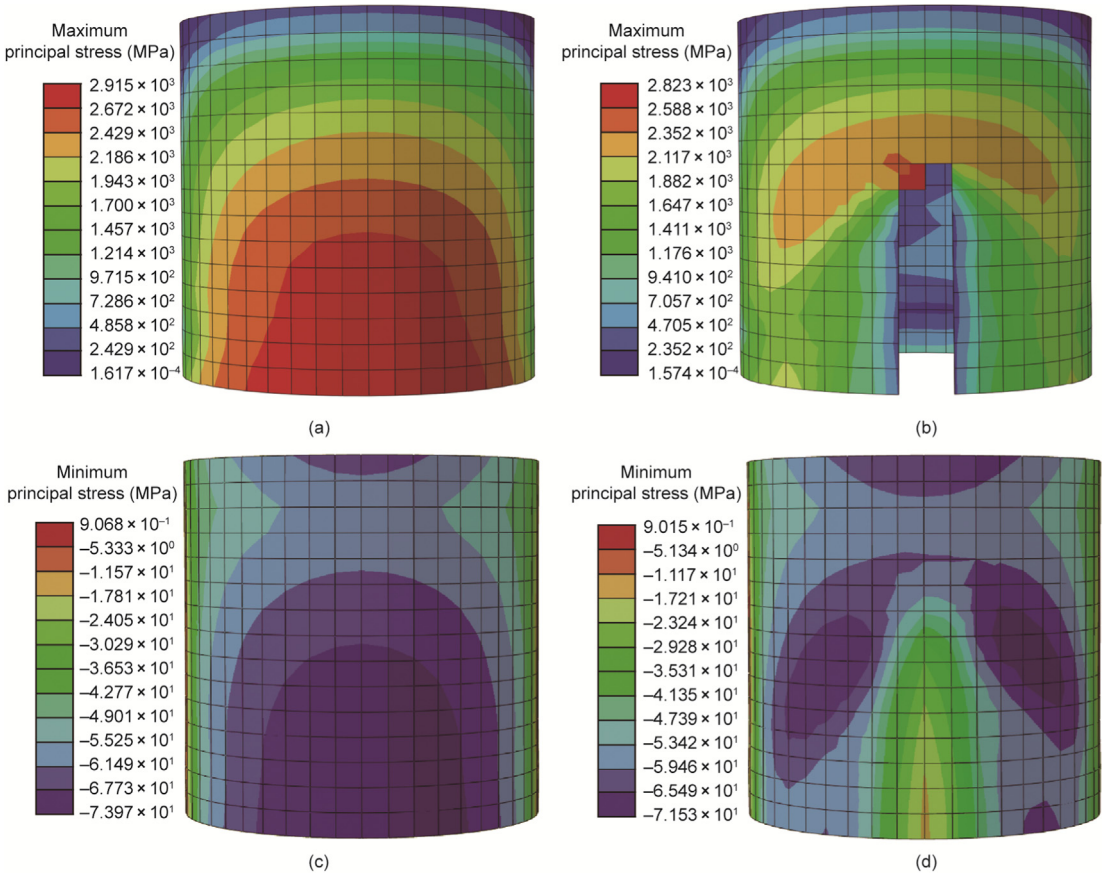

Fig. 11. Predicted failure modes for specimen L2E40A [51,52]: (a) FRP before rupture; (b) FRP after rupture; (c) concrete before rupture; and (d) concrete after rupture.

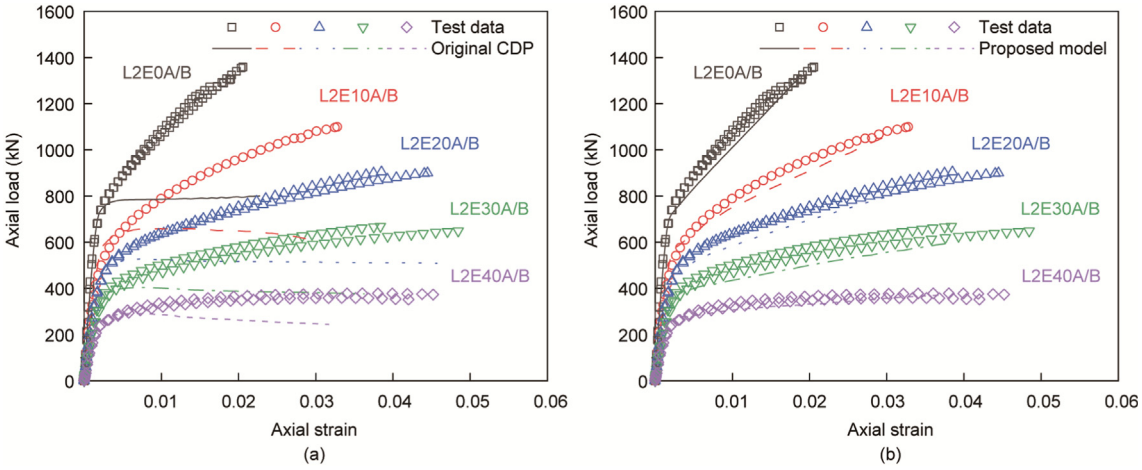

Fig. 12. Predicted versus test load–axial strain relationship at extreme compression fiber of mid-height section for FRP-confined cylinder specimens [51,52] under different eccentricities. (a) Predictions by the original CDP model; (b) predictions by the proposed model.

(2) The proposed potential surface, formed by a D–P-type and a capped surface, handled both tension and compression-dominated stress states.

(3) The evolution of the deviatoric trace of the potential surface was linked to that of the yield surface, providing reasonable predictions of non-uniform dilation while streamlining the formulation.

(4) The evolution of the compressive internal state variable was scaled by a ductility measure to account for strain enhancement due to confinement. An explicit relationship between ductility and confinement measures was established.

(5) Critical model parameters exhibited clear physical implications and were calibrated easily using test data or empirical formulae for unconfined and (actively/passively) confined concrete.

These modifications enabled the proposed model to accurately capture the mechanical behavior of confined concrete under various stress states, including plastic volumetric compaction,

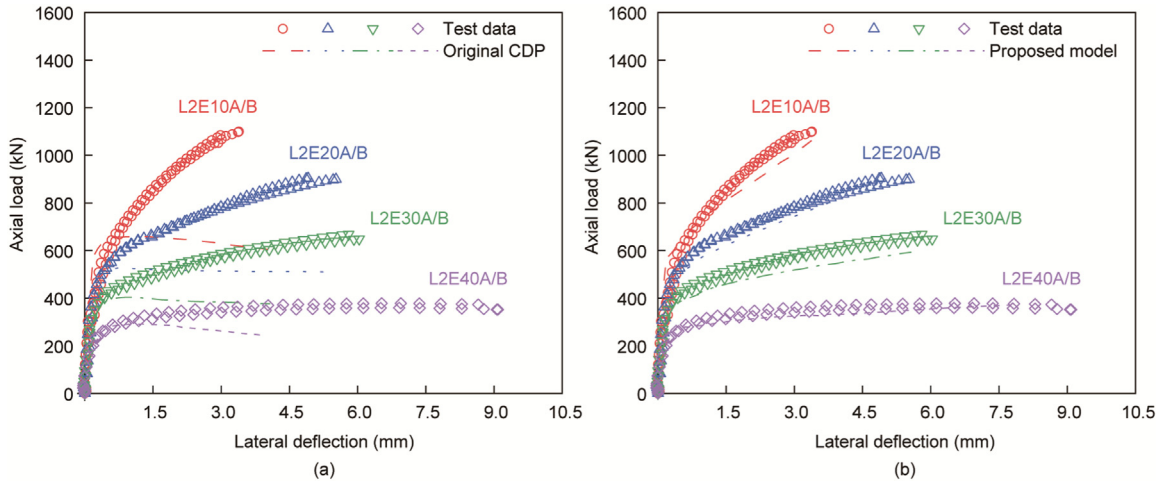

Fig. 13. Predicted versus test load-lateral deflection relationship for FRP-confined cylinder specimens [51,52] under different eccentricities. (a) Predictions by the original CDP model; (b) predictions by the proposed model.

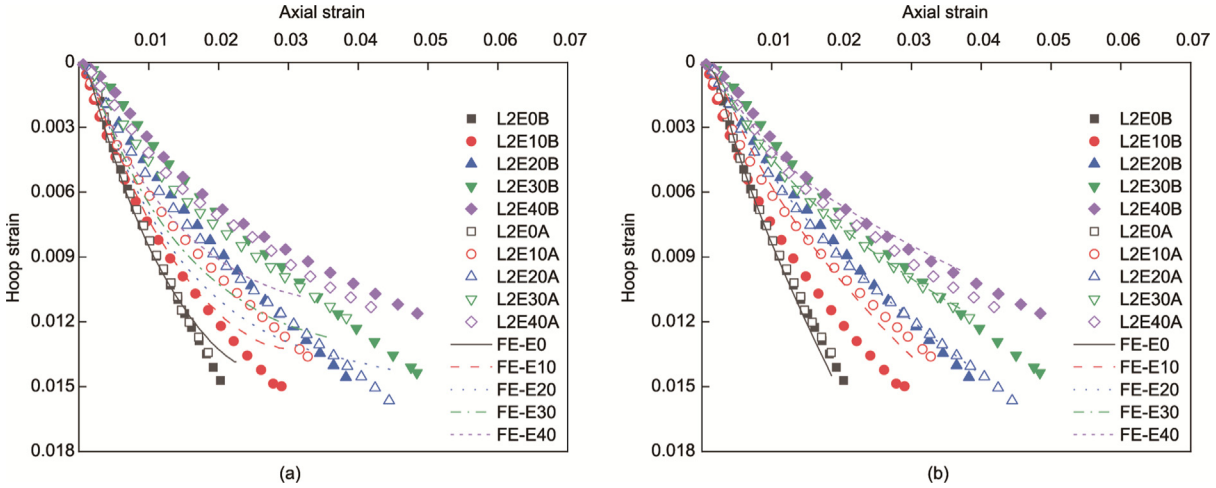

Fig. 14. Predicted versus test axial–lateral strain relationship at extreme compression fiber of mid-height section for FRP-confined cylinder specimens [51,52] under different eccentricities. (a) Predictions by the original CDP model; (b) predictions by the proposed model.

Table 8
Comparison of key test and predicted results for FRP-confined concrete specimens.

References	Specimen	Load capacity (kN) (Test)	Load capacity (kN) (FE)	Error (%)	Ultimate deflection (mm) (Test)	Ultimate deflection (mm) (FE)	Error (%)
Zhang [51] and Jiang et al. [52]	L2E0A/B	1332.7	1310.1	–1.70	–	–	–
	L2E10A/B	1092.1	1060.7	–2.88	3.22	3.37	4.66
	L2E20A/B	902.0	866.6	–3.92	5.22	4.92	–5.75
	L2E30A/B	658.3	592.9	–9.93	5.92	5.56	–6.08
	L2E40A/B	362.6	371.0	2.32	9.32	7.74	–16.95

Error (%) = [(FE result – Test result) / Test result] × 100. "Test" represents the test results that are averaged over nominally identical specimens; "FE" denotes finite element results obtained using the proposed model.

non-uniform confinement, tension-dominated stress states, and stiffness degradation. Validation under various loading conditions demonstrated the capability, rationality, and accuracy of the model. Thus, the proposed model can be readily applied to simulating more complex structural forms incorporating confined concrete, such as CFFT and DSTC columns.

Despite improved performance, the complex formulation of the proposed model can cause convergence challenges. Replacing an increment step with smaller substeps improves convergence but increases computational time. Therefore, further research is required to enhance the convergence and efficiency of the plastic return algorithm.

CRediT authorship contribution statement

Yichen Lu: Writing – original draft, Visualization, Validation, Software, Methodology, Investigation, Formal analysis, Data curation. **Guangming Chen:** Writing – review & editing, Supervision, Resources, Project administration, Methodology, Investigation, Funding acquisition, Conceptualization.

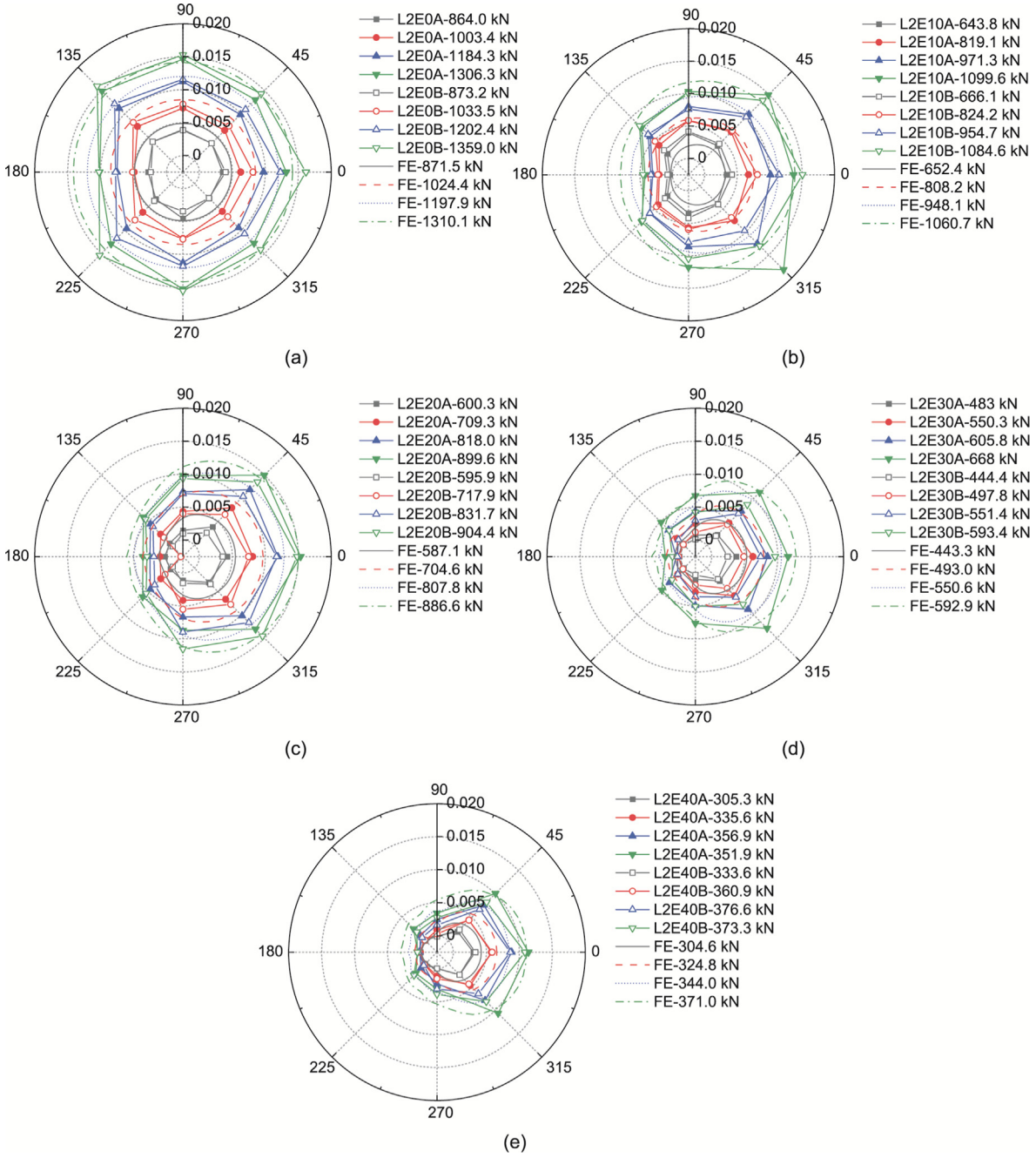

Fig. 15. Predicted versus test hoop strain distributions at mid-height section for FRP-confined cylinder specimens [51,52] under different eccentricities: (a) 0 mm; (b) 10 mm; (c) 20 mm; (d) 30 mm; and (e) 40 mm.

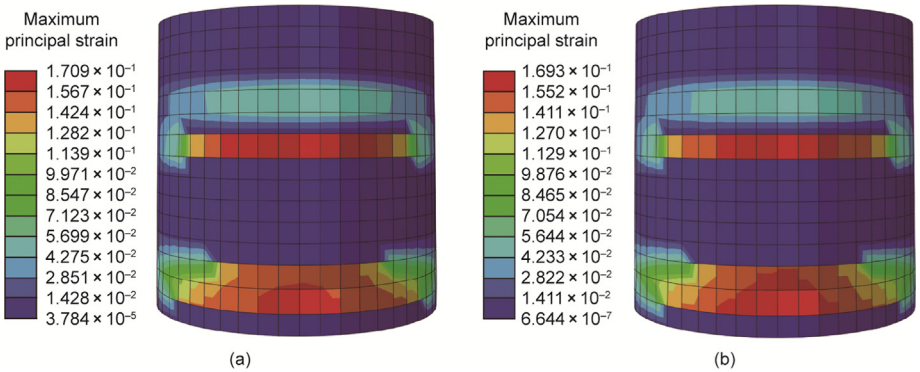

Fig. 16. Simulated axial tensile cracking at FRP rupture in FRP-confined cylinder specimen L2E40A [51,52]. (a) FRP; (b) concrete.

Declaration of competing interest

The authors declare that they have no known competing financial interests or personal relationships that could have appeared to influence the work reported in this paper.

Acknowledgements

The authors are grateful for the financial support received from the National Natural Science Foundation of China (52378156 and 51978281), the Guangdong Basic and Applied Basic Research Foundation (2024A1515012614), and the Guangdong Provincial Key Laboratory of Modern Civil Engineering Technology (2021B1212040003). The authors are grateful for the help (discussions in person or via online meetings) provided by Dr. Botong Zheng from the University of Southern California during the early stages of this work.

Appendix A. Supplementary data

Supplementary data to this article can be found online at https://doi.org/10.1016/j.eng.2026.04.003.

References

[1] Han LH, Li W, Bjorhovde R. Developments and advanced applications of concrete-filled steel tubular (CFST) structures: members. J Constr Steel Res 2014;100:211–28.
[2] Mirmiran A, Shahawy R. Behavior of concrete columns confined by fiber composites. J Struct Eng 1997;123(5):583–90.
[3] Ozbakkaloglu T, Lim JC, Vincent T. FRP-confined concrete in circular sections: review and assessment of stress–strain models. Eng Struct 2013;49:1068–88.
[4] Chen GM, He JL, Zheng BT. Local FRP cracking and global structural behavior of stub concrete-filled FRP tubes under concentric and eccentric compression. J Compos Constr 2024;28(6):04024069.
[5] Lam L, Teng JG. Design-oriented stress–strain model for FRP-confined concrete. Constr Build Mater 2003;17(6–7):471–89.
[6] Mander JB, Priestley MJN, Park R. Theoretical stress–strain model for confined concrete. J Struct Eng 1988;114(8):1804–26.
[7] Teng JG, Huang YL, Lam L, Ye LP. Theoretical model for fiber-reinforced polymer-confined concrete. J Compos Constr 2007;11(2):201–10.
[8] Yu T, Teng JG, Wong YL, Dong SL. Finite element modeling of confined concrete-I: Drucker–Prager type plasticity model. Eng Struct 2010;32(3):665–79.
[9] Yu T, Teng JG, Wong YL, Dong SL. Finite element modeling of confined concrete-II: plastic-damage model. Eng Struct 2010;32(3):680–91.
[10] Zheng BT, Teng JG. A plasticity constitutive model for concrete under multiaxial compression. Eng Struct 2022;251:113435.
[11] Richart FE, Brandtzæg A, Brown RL. A study of the failure of concrete under combined compressive stresses. Technical report. Champaign: University of Illinois at Urbana-Champaign; 1928.
[12] Richart FE, Brandtzæg A, Brown RL. Failure of plain and spirally reinforced concrete in compression. Technical report. Champaign: University of Illinois at Urbana-Champaign; 1929.
[13] Lim JC, Ozbakkaloglu T. Investigation of the influence of the application path of confining pressure: tests on actively confined and FRP-confined concretes. J Struct Eng 2015;141(8):04014203.
[14] Lee JH, Fenves GL. Plastic-damage model for cyclic loading of concrete structures. J Eng Mech 1998;124(8):892–900.
[15] Papanikolaou VK, Kappos AJ. Confinement-sensitive plasticity constitutive model for concrete in triaxial compression. Int J Solids Struct 2007;44(21):7021–48.
[16] Grassl P, Xenos D, Nyström U, Rempling R, Gylltoft K. CDPM2: a damage-plasticity approach to modelling the failure of concrete. Int J Solids Struct 2013;50(24):3805–16.
[17] de Souza Neto EA, Peric D, Owen DR. Computational methods for plasticity: theory and applications. Hoboken: John Wiley & Sons; 2011.
[18] Karabinis AI, Kiousis PD. Effects of confinement on concrete columns: plasticity approach. J Struct Eng 1994;120(9):2747–67.
[19] Mirmiran A, Zagers K, Yuan WQ. Nonlinear finite element modeling of concrete confined by fiber composites. Finite Elem Anal Des 2000;35(1):79–96.
[20] Shahawy M, Mirmiran A, Beitelman T. Tests and modeling of carbon-wrapped concrete columns. Compos Pt B Eng 2000;31(6–7):471–80.
[21] Karabinis AI, Rousakis TC. Concrete confined by FRP material: a plasticity approach. Eng Struct 2002;24(7):923–32.
[22] Rousakis TC, Karabinis AI, Kiousis PD, Tepfers R. Analytical modelling of plastic behaviour of uniformly FRP confined concrete members. Compos Pt B Eng 2008;39(7–8):1104–13.
[23] Mahfouz I, Rizk T, Sarkani S. An innovative FRP confining system for repairing rectangular columns. In: Proceedings of the Annual Conference of the American-Society-of-Civil-Engineering; 2001 Oct 10–13; Houston, TX, USA. New York City: American Society of Civil Engineers (ASCE); 2001. p. 16–25.
[24] Dassault Systemes Simulia Corp. ABAQUS analysis user's manual, version 6.5. Johnston: Dassault Systemes Simulia Corp.; 2004.
[25] Mohammadi M, Wu YF. Triaxial test for concrete under non-uniform passive confinement. Constr Build Mater 2017;138:455–68.
[26] Hany NF, Hantouche EG, Harajli MH. Finite element modeling of FRP-confined concrete using modified concrete damaged plasticity. Eng Struct 2016;125:1–14.
[27] Mohammadi M, Wu YF. Modified plastic-damage model for passively confined concrete based on triaxial tests. Compos Pt B Eng 2019;159:211–23.
[28] Farahmandpour C, Dartois S, Quiertant M, Berthaud Y, Dumontet H. A concrete damage-plasticity model for FRP confined columns. Mater Struct 2017;50(2):156.
[29] Dassault Systemes Simulia Corp. ABAQUS user documentation. Johnston: Dassault Systemes Simulia Corp.; 2018.
[30] Menetrey P, Willam KJ. Triaxial failure criterion for concrete and its generalization. ACI Struct J 1995;92(3):311–8.
[31] Lubliner J, Oliver J, Oller S, Oñate E. A plastic-damage model for concrete. Int J Solids Struct 1989;25(3):299–326.
[32] William KJ, Warnke EP. Constitutive model for the triaxial behavior of concrete. In: Proceedings of Concrete Structures Subject to Triaxial Stresses; 1974 May 17–19; Bergamo, Italy. Zurich: International Association for Bridge and Structural Engineering; 1974. p. 1–30.
[33] Lei B, Qi TY, Li Y, Jin ZY, Qian WP. An enhanced damaged plasticity model for concrete under cyclic and monotonic triaxial compression. Eur J Mech A, Solids 2023;100:104999.
[34] Pietruszczak S, Jiang J, Mirza F. An elastoplastic constitutive model for concrete. Int J Solids Struct 1988;24(7):705–22.
[35] Etse G, Willam K. Fracture energy formulation for inelastic behavior of plain concrete. J Eng Mech 1994;120(9):1983–2011.
[36] Rudnicki JW, Rice J. Conditions for the localization of deformation in pressure-sensitive dilatant materials. J Mech Phys Solids 1975;23(6):371–94.
[37] Bazant ZP. Endochronic inelasticity and incremental plasticity. Int J Solids Struct 1978;14(9):691–714.
[38] Chaboche J, Lemaitre J. A nonlinear model of creep-fatigue damage cumulation and interaction. In: Proceeding of IUTAM Symposium of Visco–elastic Media and Bodies; 1974 Sep 2–6; Gothenburg, Sweden. Gotenbourg: Springer-verlag; 1974. p. 291–301.
[39] American Concrete Institute (ACI) Committee. Building code requirements for structural concrete (ACI 318–05) and commentary (ACI 318R–05). Farmington Hills: ACI; 2005.
[40] Birtel V, Mark P. Parameterised finite element modelling of RC beam shear failure. In: Proceedings of the ABAQUS users' conference; 2006 May 23–26; Cambridge, MA, USA. Johnston: Dassault Systemes Simulia Corp.; 2006.
[41] Chen GM, Teng JG, Chen JF. Finite-element modeling of intermediate crack debonding in FRP-plated RC beams. J Compos Constr 2011;15(3):339–53.
[42] Hordijk DA. Local approach to fatigue of concrete [dissertation]. Delft: Delft University of Technology; 1991.
[43] Bažant ZP, Planas J. Fracture and size effect in concrete and other quasibrittle materials. New York City: Routledge; 2019.
[44] Comite Euro-International Du Beton. CEB–FIP model code: design code 1990. Leeds: Emerald Publishing Limited; 1993.
[45] Jiang T, Teng JG. Analysis-oriented stress–strain models for FRP-confined concrete. Eng Struct 2007;29(11):2968–86.
[46] Chen GM, Teng JG, Chen JF, Xiao QG. Finite element modeling of debonding failures in FRP-strengthened RC beams: a dynamic approach. Comput Struc 2015;158:167–83.
[47] Chen LH, Liu DW, Lei M, Zhang Y, Zhao TE, Zheng YP. The study on the constitutive model of concrete for explicit dynamic of ABAQUS based on damage energy. Adv Mater Sci Eng 2022;2022(1):1914314.
[48] Imran I. Applications of non-associated plasticity in modelling the mechanical response of concrete [dissertation]. Ontario: University of Toronto; 1996.
[49] Imran I, Pantazopoulou SJ. Plasticity model for concrete under triaxial compression. J Eng Mech 2001;127(3):281–90.
[50] Lam L, Teng JG, Cheung CH, Xiao Y. FRP-confined concrete under axial cyclic compression. Cem Concr Compos 2006;28(10):949–58.
[51] Zhang XQ. Experimental study of stress–strain behavior of FRP-confined concrete subjected to eccentric compression [dissertation]. Hangzhou: Zhejiang University; 2014. Chinese.
[52] Jiang T, Zhang XQ, Yao J, Luo YZ. Stress–strain behaviour of FRP-confined concrete subjected to eccentric compression. In: Proceedings of the 13th International Symposium on Structural Engineering (ISSE-13); 2014 Oct 24–27; Hefei, China. Hefei: Hefei University of Technology; 2014. p. 441–9. Chinese.
[53] Hashin Z, Rotem A. A fatigue failure criterion for fiber reinforced materials. J Compos Mater 1973;7(4):448–64.